The formation and dynamics of the cold-dome off northeastern Taiwan

Mao-Lin Shen [a,1], Yu-Heng Tseng [a,*], Sen Jan [b,2]

[a] Department of Atmospheric Sciences, National Taiwan University, No.1, Sec. 4, Roosevelt Rd., Taipei 106, Taiwan
[b] Institute of Oceanography, National Taiwan University, No.1, Sec. 4, Roosevelt Rd., Taipei 106, Taiwan

ARTICLE INFO

ABSTRACT

The cold-dome off northeastern Taiwan is commonly observed by remote-sensing of Sea Surface Temperature (SST) and in-situ observation. The recent remote-sensing SST and subsurface Argo profiles were analyzed to investigate possible formation mechanisms and dynamics. The observed time series of SST anomaly suggested that the surface cold-dome occurred more frequently in summer, including an unusual contribution due to the cold water residual associated with typhoon events. Subsurface hydrographic features from Argo float data indicated that the near-shore thermocline can be lifted up about 85 m by Kuroshio dynamics, and the cold saline deep water (100 m deep off northeastern Taiwan) can only result from subsurface Kuroshio. We examined the possible formation mechanisms using a duo-grids North Pacific Ocean model (DUPOM) with a horizontal resolution of 1/8° for the East Asian Seas and 1/4° for the remaining North Pacific. The model reproduced several cold-dome formation events and displayed typical cold-dome features. Further analysis shows that the geostrophic component of Kuroshio transport is the main contributor to the cold-dome formation (57.4% of the total isotherm uplift) and dominates seasonal occurrence of the cold-dome. The contribution resulting from the associated cyclonic eddy is only 3.3% of the total isotherm uplift. Additional sensitivity tests suggested that the remaining contribution (39.6% of the total isotherm uplift) is mainly due to the topographically controlled upwelling in this region. Moreover, the local boundary Ekman transport may enhance the surface appearance of the cold-dome, but plays only a minor role.

© 2011 Elsevier B.V. All rights reserved.

1. Introduction

The circulation and air–sea exchange in the southern East China Sea (ECS) and their interaction with the regional current system due to complex bathymetry and continental shelves is not completely understood. A well-known complexity exists off northeastern Taiwan, where a cold-dome associated with a cyclonic eddy (Chuang et al., 1993; Hsueh, 2000) is commonly observed. The properties of the cold-dome have been documented extensively through field surveys (for example, Tang and Tang, 1994; Tang et al., 2000; Tang et al., 1999), satellite remote sensing (for example, Cheng et al., 2009; Gong et al., 1992; Lin et al., 1992), and numerical studies (Wu et al., 2008a). Importantly, the water in this area is nutrient-rich due to the upwelling in the cold-dome (Chen, 1996; Chen et al., 2003; Hsu, 2005), and is regarded as one of the primary fishing grounds around Taiwan. The complex circulation also contributes substantially to the exchange of water mass, heat, and salinity of the ECS, Taiwan Strait Water (TSW), and Kuroshio (Chen and Sheu, 2006; Hsueh, 2000; Isobe, 2008; Matsuno et al., 2009). Therefore, a better understanding of the cold-dome formation and its interaction with regional circulation is crucial and requires more knowledge of nutrient sources and the associated water exchange in this region.

Satellite remote sensing data show that the cold-dome normally occurs on the Mien-Hua Canyon (MHC), where the temperatures are lower than the surrounding waters by about 3–6 °C, and is observed more frequently in summer than in winter (Cheng et al., 2009). Because the Kuroshio axis east of Taiwan migrates seasonally, seaward in summer and shoreward in winter (Tang et al., 2000), the variation in cold-dome occurrence may be linked to the Kuroshio. However, the cold surface temperatures in winter may reduce the possible cold-dome recognition (Liu et al., 1992), and the surface buoyancy change due to the precipitation carried by frequent typhoon events can induce the upwelling of subsurface water (Chen et al., 2003) and thus enhance its seasonal appearance. Furthermore, hydrographic surveys northeast of Taiwan show that Kuroshio Tropical Water (KTW, or Kuroshio Subsurface Water), characterized by a salinity maximum, is commonly upwelled onto the continental shelf all year round (Chuang and Liang, 1994; Hsueh et al., 1992; Hsueh et al., 1993; Liu et al., 1995; Liu et al., 1992; Wong et al., 1991) and forms the basis of the surface cold-dome (see Table 1 for the abbreviations and the associated Nomenclatures of the water masses used hereafter). The upwelling of KTW shows similar seasonal

* Corresponding author. Tel.: +886 2 33663918; fax: +886 2 23633642.
  E-mail addresses: earnestshen@gmail.com (M.-L. Shen), yhtseng@as.ntu.edu.tw
(Y.-H. Tseng), senjan@ntu.edu.tw (S. Jan).
[1] Tel.: +886 2 33663921.
[2] Tel.: +886 2 33669874.

Table 1
The abbreviations and associated nomenclatures of the water masses.

Abbreviation	Nomenclature
CCW	China Coast Water
CW	Continental Water
KSW	Kuroshio Surface Water
KTW	Kuroshio Tropical Water, or Kuroshio Subsurface Water
TSW	Taiwan Strait Water

variations with Kuroshio migration; KTW carries more water mass onto the continental shelf in summer than in winter (Chen et al., 1995).

The cold-dome is often accompanied with a cyclonic eddy off northeastern Taiwan. The eddy may be arose through the upwelling-induced buoyancy wave constrained by the associated Rossby radius of deformation and acts like a pseudo-wall, blocking the advection of warm water from TSW (Tang et al., 2000; Chuang et al., 1993; Tang and Tang, 1994; Tang et al., 2000; Tang et al., 1999). However, the surface eddy may also be introduced by the island wake instability, as the flow found on the lee side of the Izu Islands (Isoguchi et al., 2009). Specifically, the characteristics of the surface cyclonic eddy are probably impacted by the surrounding asymmetric flow strength, as contributed by the TSW and Kuroshio and its variations. This flow enhanced cyclonic motion can feed more cold water into the cold-dome and its contribution will be verified numerically.

In addition to the cyclonic eddy, local wind effects could contribute to the formation of the cold-dome. Gong et al. (1992) reported that the disappearance of the cold-dome in summer was associated with the summer monsoon. Recently, Chang et al. (2009) showed that the upwelling introduced by Kuroshio is much larger than the effects of Ekman pumping based on an eddy-resolving numerical model. Furthermore, Chang et al. (2010) applied a simplified heat budget equation to investigate the temperature change due to Ekman transport and surface heat flux for the case of surface current against wind direction. This explained the variations in the wind stresses of Peng-Chia Yu and sea surface temperatures (SST) of Long-Tung buoy; however, the seasonal appearance of the cold-dome, particularly the major occurrence in summer, is still unanswered when this method is applied.

In addition to a local wind adjustment, the precipitation and surface wind carried by typhoons may also induce the cold-dome pattern. Chen et al. (2003) observed the nutrient enhancement after the passage of Typhoon Herb in July 1996 and demonstrated that the buoyancy flux increase due to typhoon precipitation would suggest an enhancement of upwelling. Typhoon-induced current velocities can further change the axis of Kuroshio (Chen et al., 2003; Morimoto et al., 2009) and may affect the cold-dome formation. Furthermore, the atmospheric cooling effects and the inertial current induced by a typhoon can last for several days after the passage of the typhoon (Wu et al., 2008b).

Based on these previous studies, a consensus has clearly not yet formed on the formation mechanisms of the cold dome. The main objective of this study was to investigate and evaluate different formation mechanisms of the cold-dome frequently observed off northeastern Taiwan. An enhanced understanding of the formation mechanisms could improve the regional prediction capability and reduce the model uncertainty. In this study, we adopted field data (Argo float data and satellite SST images) to examine properties of the cold-dome off northeastern Taiwan. The cold-dome formation was then studied numerically by a basin-scale, eddy-resolving dual-domain Pacific Ocean Model (DUPOM), which well resolved the Kuroshio, and provided a greater understanding of the regional ocean dynamics in the vicinity of northeastern Taiwan (Tseng et al., 2011; Jan et al., 2010). We evaluated the major and other secondary contributions to the cold-dome formation by analyzing several

potential mechanisms in the model, such as geostrophic adjustment uplift, topographic upwelling, and turbulent mixing as well as Ekman boundary transport.

This paper is organized as follows. Section 2 provides the temporal characteristics of the surface cold-dome and subsurface variation of hydrographic properties to investigate the physical processes occurring in the cold-dome. Section 3 describes the numerical model, DUPOM. Section 4 contains a numerical analysis of the properties and possible mechanisms of cold-dome formation. Section 5 discusses the contributions of different formation mechanisms. The conclusions are addressed in Section 6.

2. Recent observations of cold-domes

Both remote-sensing data and Argo floats were used to quantify the surface and subsurface behaviors of the cold-dome. We mainly focused on the area off northeastern Taiwan from 120ºE, 24ºN to 124ºE, 28ºN, as shown in Fig. 1(a). The merged SST data from both microwave (MW) and infrared (IR) remote sensing were used to analyze the spatial and temporal variation of SST off northeastern Taiwan, and provide some surface evolution for the cold-dome formation. The MW and IR merged SST data were obtained from Remote Sensing Systems (available at www.remss.com). High resolution MW and IR merged SST data are available at a $0.09° \times 0.09°$ spatial resolution over the global region ($\pm 90°$). Daily mean SST data were used.

For the subsurface data, we analyzed the temperature and salinity distribution from the Argo profiles, which are quality-controlled through USGODAE (Global Ocean Data Assimilation Experiment, www.usgodae.org). The Argo floats have been deployed over the world's oceans, and have provided reliable measurements of temperature and salinity profiles of the upper 2000 m of the ocean. The temperature measurement is reliable (accuracy: ~10^{-3} °C) and the surface temperature is usually used to calibrate the remote-sensing SST (Udaya Bhaskar et al., 2009). Note that no continuous daily Argo data are available, and therefore a time series analysis for Argo data at a specific location is difficult.

2.1. Spatial patterns of SST during the cold-dome events

Satellite SSTs for 2008 and 2009 were studied; 731 daily data were acquired and the cold-dome was found in 84 of them (11.5%). Normally, the temperature inside the cold-dome is more than 3 °C lower than that of the surroundings in summer. In winter, this difference is rarely observed because the surrounding water is also cold and the temperature difference is not so significant. Fig. 2 shows four typical spatial patterns of SST distribution when a cold-dome was observed (images are taken from May 16, 2008; July 30, 2008; May 2, 2009; and November 7, 2009). According to Cheng et al. (2009) (their Fig. 6), the center of the cold-dome off northeastern Taiwan is usually restricted to isobaths east of 100 m and west of 1000 m. The dark-red encircled region in Fig. 2 was chosen by this criterion and is termed the Cold-Dome Favorable Region (CDFR) hereafter. In these representative images, the fronts, resulting from the large temperature gradient, are clearly detected between warm Kuroshio water and cold Continental Water (CW). In particular, the edge of Kuroshio, similarly to those shown in the paper of Lin et al. (1992), can be identified clearly in all panels of Fig. 2, except panel (b). Fig. 2(b) presents a different frontal pattern, where the surface flow was strongly affected by the category 2 typhoon (on the Saffir-Simpson scale) Fung-Wong, whose center was located at 121°E, 24.1°N on July 28, 2008 and which had a radius of approximately 220 km. These patterns imply some different formation mechanisms for the cold-dome, suggesting a highly complicated circulation pattern in this region. More details are discussed later.
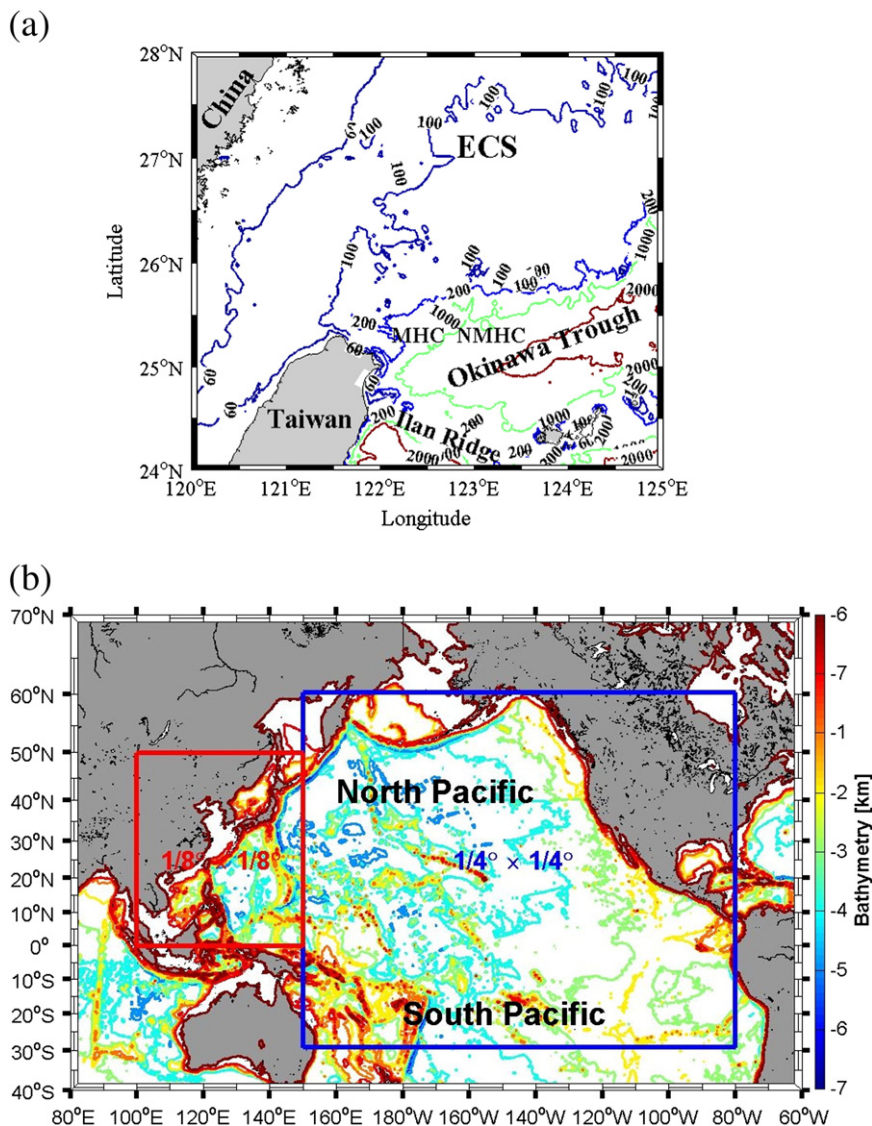
Fig. 1. (a) Domain of interest in this study. Some key regions are noted, such as the East China Sea (ECS), Mien-Hua Canyon (MHC), North Mien-Hua Canyon (NMHC), Okinawa Trough, and Ilan Ridge unit of contour is the meter; (b) Schematic of the full simulation domain. The right NPB domain covers the eastern Pacific from 150°E, 30°S to 80°W, 60°N with a horizontal grid resolution of 1/4° while the left TAI domain covers the western Pacific from 100°E, 0°S to 150°E, 50°N with a finer horizontal grid resolution of 1/8°. The bathymetry contour interval is 1000 m.

2.2. Temporal SST variation during 2008–2009

To analyze the occurrence of cold-dome events, the time evolution of the meridionally averaged SST anomaly (SSTA) during 2008–2009 is shown in Fig. 3 (120–124°E), in which the seasonal influences were eliminated by a high-pass filter. The line at 122°E (solid line) represents the typical cold-dome center off northeastern Taiwan. Fig. 3 shows the zonal span of SSTA versus time. The cold-dome was primarily observed from May to October, consistent with the typical Kuroshio offshore period suggested by Tang et al. (2000). This seasonal appearance of the cold-dome agrees well with that proposed by Wu et al. (2008a) and Cheng et al. (2009) and indicates the formation of the cold-dome is strongly influenced by the surrounding flow pattern, such as Kuroshio migration, Taiwan Strait outflow, and the cyclonic eddy. With more inshore Kuroshio intrusion in winter, strong fronts are often found at about 122°E along the continental slope, and hence identifying the cold-domes from the SSTA is more difficult.

Various cool SSTA events with a large zonal span exist in the area of interest and have a long duration. For example, an extended cool SSTA is observed during the middle of August 2009, resulting from Typhoon Morakot on August 8, 2009. The typhoon introduced an extreme

rainfall event (more than 1 m per day over southern Taiwan) and changed the surface hydrographic features, freshening and cooling the ocean surface, particularly upstream of Kuroshio. The surface cooling mechanism due to the passage of typhoons has been previously documented (Chen et al., 2003; Tseng et al., 2010; Wu et al., 2008b; Zheng et al., 2010). According to the filtered SST data, we observed that the cold water off northern Taiwan remained for more than a week, which suggests more negative heat flux into the surrounding atmosphere, potentially influencing the regional climate.

Although the winter Kuroshio intrusion (the main axis moving inshore) is well-documented, interannual variation of the Kuroshio front exists. In 2008, the Kuroshio front reached approximately 121.8°N in February and retreated after mid-May. However, the retreated front in early February, 2009 introduced a cold-dome lasting for a few days. This suggests that the Kuroshio migration varies with time and the cold-dome formation is strongly influenced by the Kuroshio.

2.3. Subsurface measures of Argo profiles

To analyze the vertical profile and distribution in the vicinity of northeastern Taiwan, we used the historical Argo profile data collected
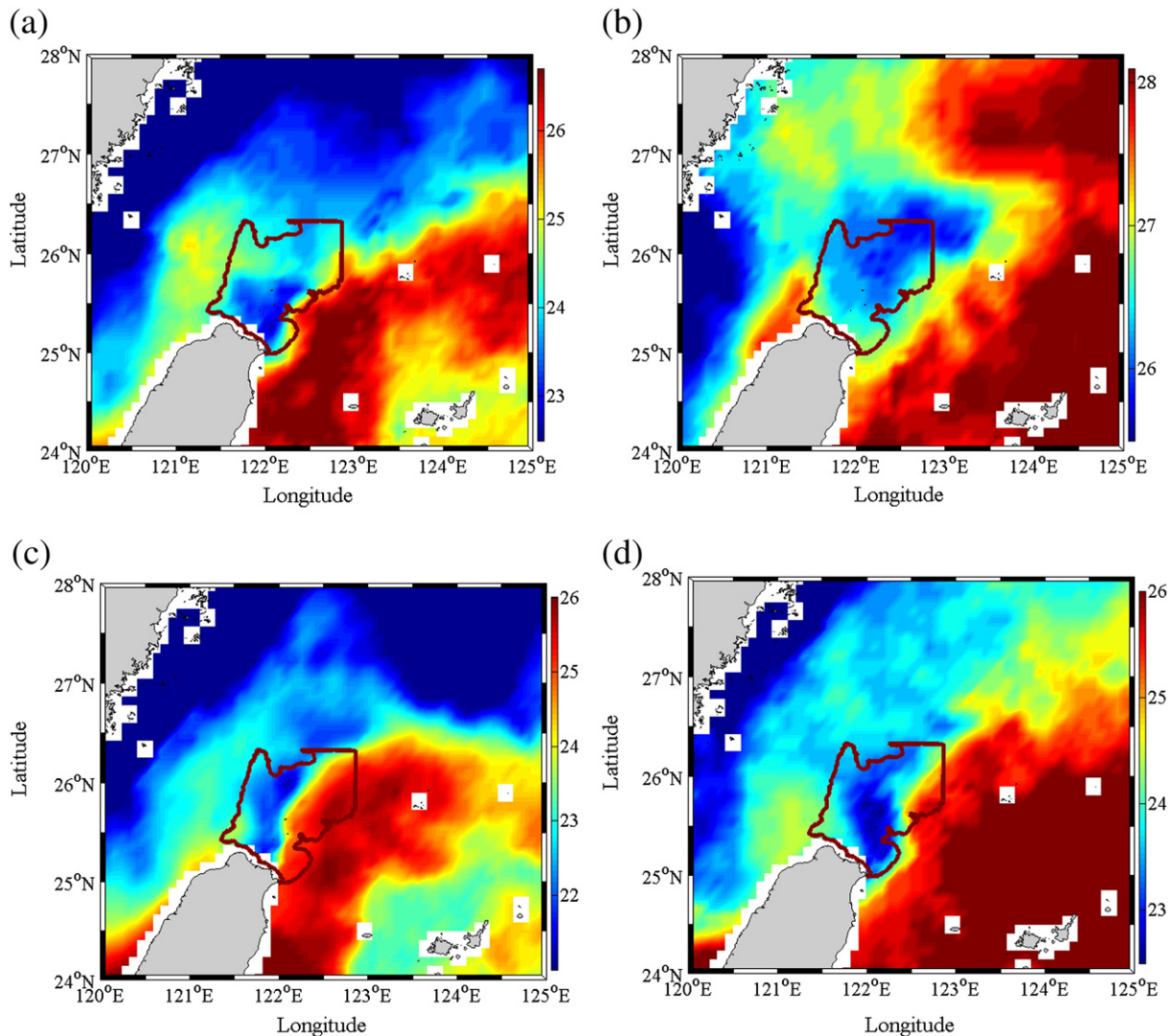
Fig. 2. The SST image around the region of interest: (a) on May 16, 2008; (b) on July 30, 2008; (c) on May 2, 2009; (d) on November 7, 2009. SST is shaded and the unit is °C. The dark-red encircled area indicates the Cold-Dome Favorite Region (CDFR). The fronts identify the boundary between warm Kuroshio water and cold Continental Water (CW).

within the domain of interest between 118°E, 22°N, and 128°E, 32°N. Fig. 4 shows the spatial distribution for nine years of Argo data from August 3, 2001 to September 4, 2009. Although there are a total of 2047 Argo floats passing through the region of interest, most of them are located in the offshore region where the bathymetry is much deeper. No Argo floats were observed in the channel of the Taiwan Strait and ECS. Only a few of them drifted onto the continental shelf with Kuroshio intrusion. The absence of Argo floats in the ECS and Taiwan Strait suggests that local cruise observation and model simulation are inevitably required to better understand the regional circulation in detail.

Of these 2047 observations, only two major groups of the region are of interest in this study. One group is located along the Kuroshio main axis, and the other group is located off northeastern Taiwan with bathymetry shallower than 400 m. According to early field observations (Tang et al., 2000), the Kuroshio axis along 25.125°N is mainly centered at about 122.75°E with a span of approximately 100 km. Therefore, we took the data within the blue box in Fig. 4 (near Ilan Ridge, 122.1°E, 24.2°N to 123.1°E, 24.7°N) to represent the Kuroshio water mass. In total, 33 Argo floats were chosen with a maximum salinity larger than 34.7 psu. This agrees well with the requirement of the Kuroshio main stream (Chuang et al., 1993). For the CDFR, only

a few Argo floats pass through this area, and so most of them are used.

Of the 33 Argo profiles taken from the Kuroshio main stream near Ilan Ridge, 21 are in summer and 12 are in winter. Fig. 4(b) and (c) shows the temperature–salinity (T–S) diagrams of Kuroshio in summer and winter, respectively. The averaged T–S profiles in the selected area were also included. Fig. 4(b) shows that the hydrographic features have a smaller variance, indicating that the Kuroshio water properties dominate. In contrast, the winter T–S diagram shows a larger variability and indicates that the winter hydrographic features are easily affected by the surrounding waters. Note that the lowest salinity of the subsurface feature with a temperature around 7 °C is higher than 34.2 psu, which is the lowest salinity in the West Philippine Sea Water (Chen and Huang, 1996). This suggests that the West Philippine Sea Water conveyed by Kuroshio is mixed with another water mass; such as the saline intermediate water (depth from 350 m to 1000 m) of the South China Sea, which flows out through the Luzon Strait with a minimum salinity of 34.45 psu (Chen and Huang, 1996; Chen, 2005, 2008).

Although Argo floats can provide useful subsurface T–S profiles, they provide minimal information about the surface temperature and no spatial information for the surface cold-dome. Therefore, Argo data
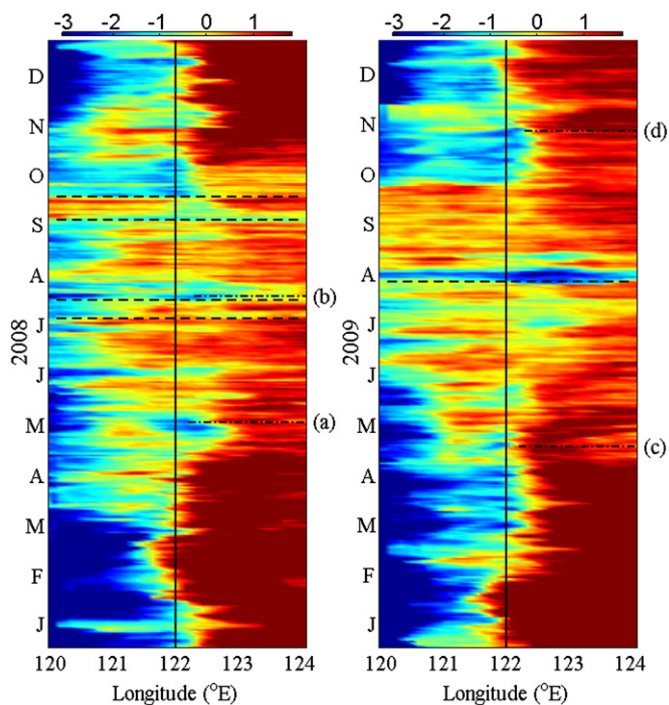
Fig. 3. Zonal-temporal plot of filtered SST north of Taiwan in 2008 (top) and 2009 (bottom). Meridionally averaged (25.4°N–25.9°N) temperature was used to show the appearance of the cold dome. The unit is °C. The typical cold-dome center northeast of Taiwan is along 122° E (horizontal solid lines). Several typhoon events are shown by dashed lines. Left: The typhoons in 2008, from left to right (dashed lines), are Kalmaegi (July 17), Fung-Wong (July 28), Sinlaku (September 14), and Jangmi (September 28), respectively. Right: The dashed line in 2009 is Typhoon Morakot (August 8). The four panels in Fig. 2 are marked by central lines, labeled as (a), (b), (c), and (d), respectively.

should be integrated with satellite images to detail the overall properties of the cold-dome. We choose two Argo floats, WMOID 2900797 and WMOID 2900819, during two typical cold-dome periods to further explore the subsurface structure of the cold-dome.

2.3.1. WMOID 2900797

All the Argo floats within the CDFR over the nine year period were checked and the Argo float WMOID 2900797 was picked because it included the hydrographic data located at the edge of a cold-dome, useful in showing clear subsurface information on the cold-dome. The Argo float data from December 4 to December 16, 2008 are shown in Fig. 5. Fig. 5(a) shows the trajectory of the float (the associated time and locations marked on the map). This Argo float shows a typical Kuroshio intrusion into the CDFR. While moving northward with Kuroshio, the float first drifted northeastward across Ilan Ridge and turned westward with the Kuroshio intrusion off northeastern Taiwan. It then floated inside the CDFR to the edge of a cold-dome (Fig. 5(b)). The near-surface temperature on December 16, shown in Fig. 5(c), was consistent with the MW and IR merged SST (21.34º C), and the actual temperature within the cold-dome was supposedly colder than this Argo float observation near the edge of the cold-dome. Fig. 5(b) also indicates that the China coastal region and the western channel of the Taiwan Strait were occupied by the China Coast (CCW) Water with the coldest SST. The cold CCW was possibly transported into the eastern part of the Taiwan Strait and flowed northward (Chen, 2003; Naik and Chen, 2008) into the CDFR. Thus, the subsurface hydrographic features are inevitably required to identify the source of the water mass.

The vertical profiles of subsurface temperature on different days of this Argo float are shown in Fig. 5(c). The associated salinity and T–S profiles are also shown in Fig. 5(d) and (e), respectively. The bold solid line indicates the hydrographic features of Kuroshio in winter as

shown in Fig. 4(c). The results show a shallower mixing layer depth (about 50 m) than the earlier observation in winter 1999 (70 m in Chang et al. (2009)). The observed 16 °C isotherm (approximately 135 m deep) was also shallower than that in the Kuroshio (220 m). This difference (roughly 85 m) is not surprising and mainly resulted from the dynamic (isotherm) uplift (Tomczak, 2000) in order to maintain the geostrophic equilibrium. Hereafter, we use "dynamic isotherm uplift" to represent the geostrophic contribution from the Kuroshio. The magnitude of dynamic isotherm uplift is determined by the geostrophic balance of Kuroshio. Moreover, the similar temperatures and salinities on December 4 and December 8 indicate that, on those days, the water masses and the associated transport along the east coast of Taiwan were mainly dominated by Kuroshio.

Strong stratification was observed when the float was drifting on the edge of the North Mien-Hua Canyon (NMHC) on December 12. The four segments in the stratification resulted from different water masses and surface mixing. The possible water masses are Kuroshio Surface Water (KSW, highest temperature), KTW (highest salinity), and TSW (lowest salinity) (Chen et al., 1995). The first layer on December 12 was above 40 m in depth and exhibited the highest temperature (24.6 °C) and lowest salinity (34.29), suggesting warm water carried by Kuroshio winter intrusion mixed with the surface CW. A similar pattern is observed from the SST distribution shown in Fig. 5(b), where the Kuroshio front (yellow colored) suggests that the KSW flowed northward against Santiao Chiao, turned westward above NMHC and then moved onto continental slope, carrying relatively warm and salty KSW mixed with CW. The second layer was between 40 m and 65 m deep and had the lowest salinity (34.17) of the four Argo data, suggesting that the water mass was mainly formed by CW. The third layer was between 70 m and 105 m deep and had the highest salinity, similar to that of KTW, suggesting that the uplifted KTW had not been mixed at the edge of CDFR. The fourth layer was below 105 m and had the lowest temperature. Of particularly note in the T–S diagram is that the water mass below the 19 °C isotherm is almost identical to that in the Kuroshio, implying that the KTW could upwell to a depth of 70 m along the continental slope. In the upper 70 m, the water mass was a mixture of Kuroshio and CW.

Note that the lowest salinity in this Argo profile was 34.17 psu, far larger than the salinity of the CCW, which has maximum salinity of about 33 psu (Chen, 2003; Naik and Chen, 2008). This indicates the cold CCW shown in Fig. 5(b) makes little contribution in the CDFR. Therefore, the possible source of the CW is the southern ECS, where the fresher ECS Water may mix with the saline KSW and be pushed southwestwardly by the northeast monsoon wind into the CDFR to form the CW in this Argo profile.

When the Argo float drifted westward, and located north of MHC on December 16, a similar stratification was shown in the Argo data. However, only three layers remained the first layer was above a depth of 60 m deep with an approximately constant temperature and salinity; the second layer was between 60 m and 75 m; the third layer was below 75 m with the lowest temperature and highest salinity. An approximately constant temperature and salinity in the first layer shows that strong vertical mixing dominates the energy transport above 60 m deep. In the second layer, a transition zone exists, mixing the cold and saline KTW in the third layer and the warmer water above. The water mass in the third layer on December 16 was less saline than that on December 12, suggesting that the original upwelled KTW has been mixed with the other water mass.

2.3.2. WMOID 2900819

Another cold-dome was observed towards the east of the CDFR during July 2008 and an Argo float passed by on July 17, 2008 (Fig. 6). This cold-dome formed directly from the passage of typhoon Kalmaegi (July 16 to July 18, 2008). Typhoon Kalmaegi was only a category 2 typhoon; however, it caused a huge amount of damage to
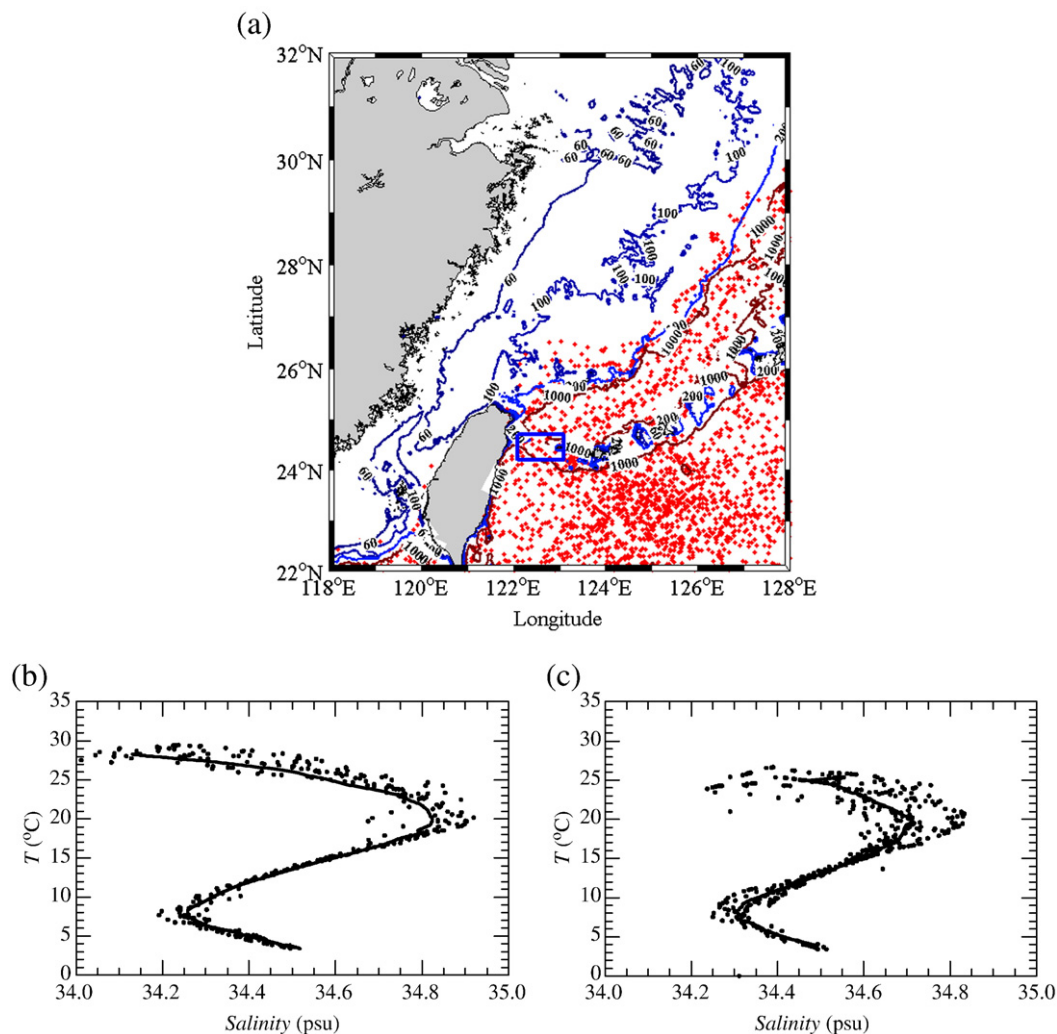
Fig. 4. (a) The Argo data from August 3, 2001 to September 6, 2009, marked as red solid circles. The blue box marks the main stream of Kuroshio on Ilan Ridge. The contours are 60, 100, 200, and 1000 m, respectively. Argo data (solid circles on (b) and (c)) collected along the Kuroshio main stream (maximum salinity larger than 34.7 psu) have 21 profiles from May to October (i.e., summer pattern (b)), and 12 profiles from November to April (i.e., winter pattern (c)). Bold solid lines are their averages.

southern Taiwan (see the track of the typhoon center every 12 h in Fig. 6(a), denoted by hollow circles). Fig. 6 shows the corresponding trajectory, MW and IR merged SST with the associated Argo float location, temperature, salinity, and T–S diagram. Fig. 6(c) shows that the offshore Kuroshio drives the float to move northeastward along the continental shelf.

The satellite image in Fig. 6(b) indicates that the cold-dome formed on July 17 in association with a large amount of surface cooling due to the influence of Typhoon Kalmaegi. Although the typhoon did not directly hit the extended cooling region, the upper ocean was significantly affected by its associated rains, largely reduced cloud cover, and intensive air–sea flux exchange. The Kuroshio and Taiwan Strait throughflow then played an important role in transporting the momentum and heat change extensively northward (Tseng et al., 2010). This resulted in a T–S diagram different to the former case. The properties of the water mass were significantly modified due to the large surface flux exchange. The upper ocean layer was restratified such that the surface mixed layer was not clear until July 24 when the restratification was completed with no further residual impacts from the typhoon. Note that the T–S diagrams for July 17 and July 20 are quite similar. The oceanic response to Typhoon Kalmaegi through complex air–sea interaction is consistent with the temporal signature in Fig. 3. For example,

energetic breaking waves, causing cold air bubbles to penetrate the subsurface, may have lasted for a long period even though the typhoon had left almost one week before.

This Argo float provides more information than expected. The dotted lines for July 24, 2008 (after the passage of Typhoon Kalmaegi) show the restratification returning to the normal conditions of Kuroshio. Further comparison of the T–S diagram and individual vertical profiles indicates two major types of water mass above and below 70 m. Above 70 m, the water mass is close to what it was on July 13, when the surface water mixed with the river inflows and rainfalls introduced by Typhoon Kalmaegi. Below 70 m, the hydrographic features show the direct contribution of KTW due to the high salinity (>34.7 psu).

A notable hydrographic feature is observed in the intermediate water, which according to the alongshore Argo profiles is a more saline water mass (thin lines) than that of the Kuroshio (bold line). This is due to the outflow of saline intermediate South China Sea Water, transported into Kuroshio (Chen, 2005, 2008) and makes the alongshore intermediate water of these Argo profiles more saline. Furthermore, this result indicates that the intermediate South China Sea Water has been transported northwardly with the Kuroshio current and has occasionally upwelled into the ECS as evidenced by Chen and Huang (1996) and Chen (2005, 2008 and 2009).
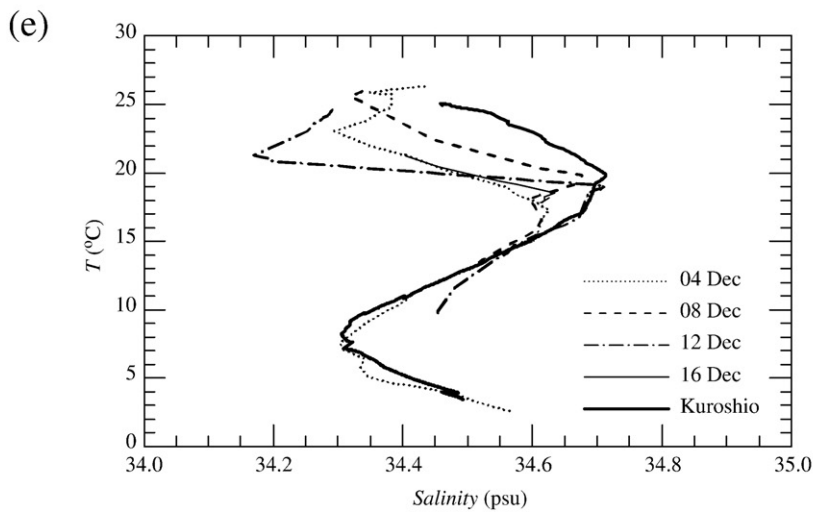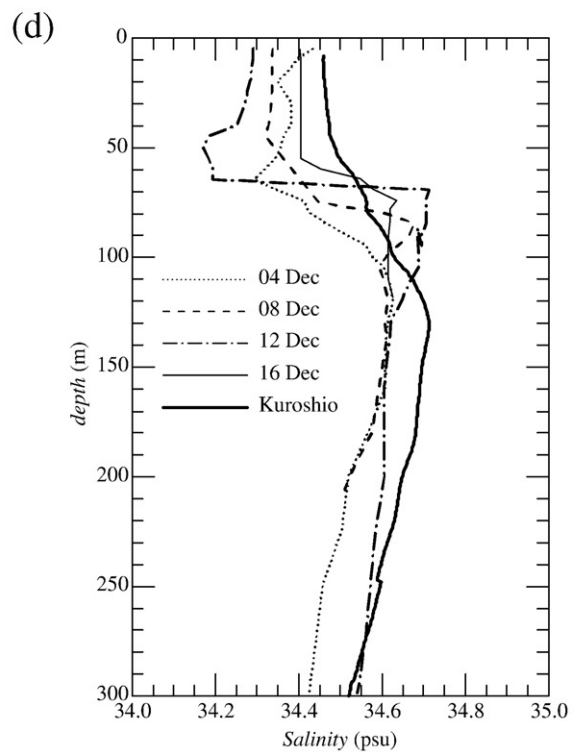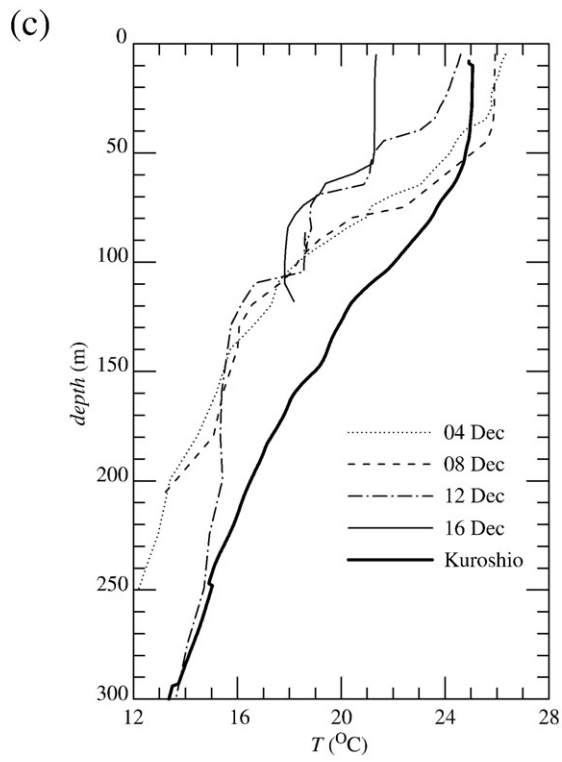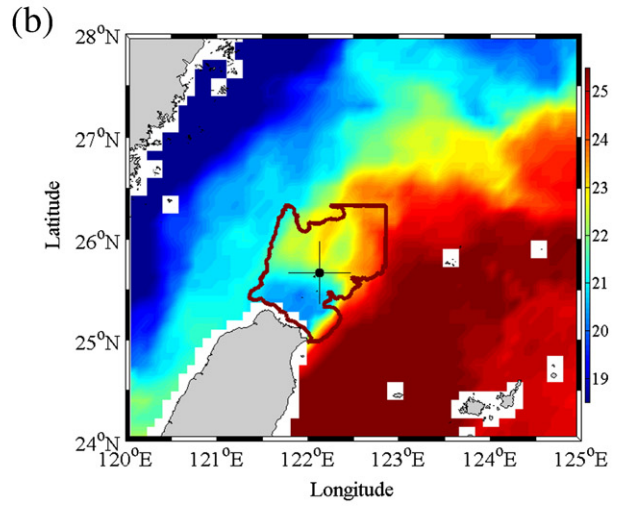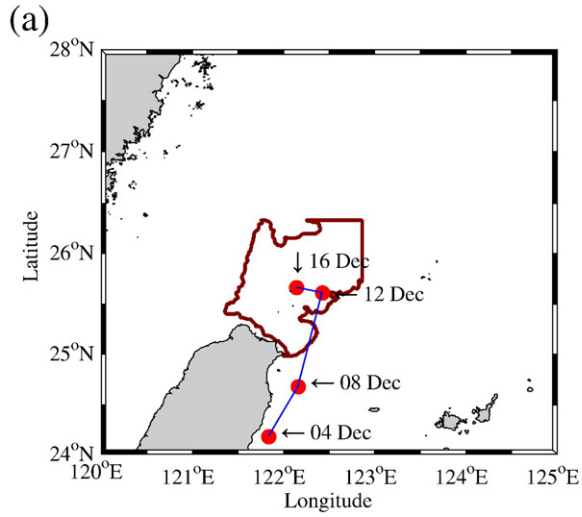
3. Numerical model

To accurately investigate the cold-dome off northeastern Taiwan, we used the hydrostatic, z-level, mixed collocated Arakawa A and C grids and fourth-order accurate DUPOM. The DUPOM is based on the Dietrich Center for Air Sea Technology (DieCAST) ocean model, and provides high computational accuracy and low numerical dissipation and dispersion (Dietrich et al., 2004; Tseng et al., 2005). The DUPOM is currently a standard configuration of the Taiwan Multi-Scale Community Ocean Model (TIMCOM), which can be used to simulate a variety of ocean dynamics using the novel multiple-domain approach (Tseng et al., 2011).

3.1. Governing equations

The governing equations are based on the three-dimensional (3D) primitive equations for an incompressible, stratified fluid in spherical coordinates. We describe the hydrostatic model using the rigid-lid and Boussinesq approximations. λ is the longitudinal variable, ϕ is the latitudinal variable, and z the vertical variable.

• Conservation of mass:

$$\frac{1}{R\cos\phi}\left(\frac{\partial u}{\partial\lambda} + \frac{\partial(v\cos\phi)}{\partial\phi}\right) + \frac{\partial w}{\partial z} = 0, \tag{1}$$

• Horizontal momentum equations:

$$\frac{\partial u}{\partial t} = -Lu + \left(f + \frac{u\tan\phi}{R}\right)v - \frac{1}{\rho_0 R\cos\phi}\frac{\partial p}{\partial\lambda} + D_m u + \frac{\partial}{\partial z}\left(A_u\frac{\partial u}{\partial z}\right), \tag{2}$$

$$\frac{\partial v}{\partial t} = -Lv - \left(f + \frac{u\tan\phi}{R}\right)u - \frac{1}{\rho_0 R}\frac{\partial p}{\partial\phi} + D_m v + \frac{\partial}{\partial z}\left(A_v\frac{\partial v}{\partial z}\right), \tag{3}$$

• Conservation of potential temperature:

$$\frac{\partial T}{\partial t} = -LT + D_h T + \frac{\partial}{\partial z}\left(K_T\frac{\partial T}{\partial z}\right), \tag{4}$$

• Conservation of dissolved salt:

$$\frac{\partial S}{\partial t} = -LS + D_h S + \frac{\partial}{\partial z}\left(K_S\frac{\partial S}{\partial z}\right), \tag{5}$$

• Hydrostatic equation:

$$\frac{\partial p}{\partial z} = -(\rho - \overline{\rho})g, \tag{6}$$

• Equation of state:

$$\rho = \rho(S, T, p), \tag{7}$$

where u and v are the velocity components in the λ and φ directions, respectively, and w is vertical velocity. S is the salinity and T is the potential temperature. f is the Coriolis parameter, ρ_0 is the mean density, $\overline{\rho}$ is the horizontal average of density at depth z, and p is the pressure. A_u and A_v are vertical eddy viscosity coefficients for horizontal momentum equations, while K_S and K_T are the vertical eddy diffusivity for salinity and temperature equations. The convection and horizontal diffusion operators L and $D_{m(h)}$ are defined as:

$$L = \frac{u}{R\cos\phi}\frac{\partial}{\partial\lambda} + \frac{v}{R}\frac{\partial}{\partial\phi} + w\frac{\partial}{\partial z}, \quad D_{m(h)} = \frac{A_{m(h)}}{R^2}\left(\frac{1}{\cos^2\phi}\frac{\partial^2}{\partial\lambda^2} - \tan\phi\frac{\partial}{\partial\phi} + \frac{\partial^2}{\partial\phi^2}\right), \tag{8}$$

where $A_{m(h)}$ is the horizontal eddy viscosity (diffusivity) coefficient for momentum (or scalar) equations. Assuming that the hydrostatic approximation is valid, the pressure field can be computed by integrating Eq. (6) from a rigid-lid surface to any depth z:

$$p = p_s + p_b, \quad p_b = g\int_z^0\rho dz, \tag{9}$$

where p_s is the surface pressure due to atmospheric or other physical phenomena.

3.2. Model description

The model domain covers the entire North Pacific Ocean ranging from 100°E to 80°W and from 30°S to 60°N; see Fig. 1(b) for the model domain and the bathymetry. To reduce the computational time, we use a duo-grid approach based on the multiple-grid framework (Dietrich et al., 2004; Dietrich et al., 2008). A 1/4° horizontal resolution is used east of 150°E (right block in Fig. 1(b), the NPB domain), while a finer horizontal resolution of 1/8° is used west of 150°E (left red block in Fig. 1(b), the TAI domain), where the Kuroshio and its associated circulations in the marginal seas are accurately resolved.

The model bathymetry is interpolated from unfiltered ETOPO-2 depth data supplemented with the 1-minute high accuracy depth archive in the Asian Seas (Liu et al., 1998) from the National Center for Ocean Research's (NCOR) of Taiwan. The vertical resolution is a linear-exponential stretched grid of 25 layers with a top layer thickness of 6 m. Both domains use the same vertical grids to avoid inconsistency. Within each domain, the longitudinal resolution is uniform and latitudinal resolution is generated such that the varying latitude and longitude grid increments are equal everywhere (Mercator grid).

The surface wind forcing is obtained from the interpolated monthly Hellerman and Rosenstein winds stress (Hellerman and Rosenstein, 1983). The Levitus94 seasonal climatology (Levitus and Boyer, 1994) is used to initialize the model and determine its surface sources of heat and fresh water using the non-damping approach. The vertical mixing is parameterized by eddy diffusivity (for temperature and salinity) and viscosity (for momentum) using a modified Richardson number dependent formula based on Pacanowski and Philander (1981). Further details about the model set-up and description can be found in Tseng et al. (2011, 2010b).

4. Numerical results

Field measurements in the vicinity of northeast Taiwan provide useful information on the properties of the cold-dome and possible dynamics. However, the lack of temporal–spatial information (particularly subsurface information) makes it difficult to analyze and investigate the detailed formation mechanisms of the cold-dome and their contribution. Here, we studied the numerically reproduced cold-dome based on an eddy-resolving DUPOM and verified the results with well-documented observations. We also applied the Lagrangian tracers to determine the role of different water sources.

Fig. 5. Argo data, WMOID 2900797, for (a) the trajectory of the float in our area of interest; (b) MW and IR merged SST (the location of the Argo float on December 16, 2008 is marked as a circle). The subsurface temperature (c), salinity (d), and T–S profiles (e) are presented, in comparison with the hydrographic features of the Kuroshio main stream in winter.
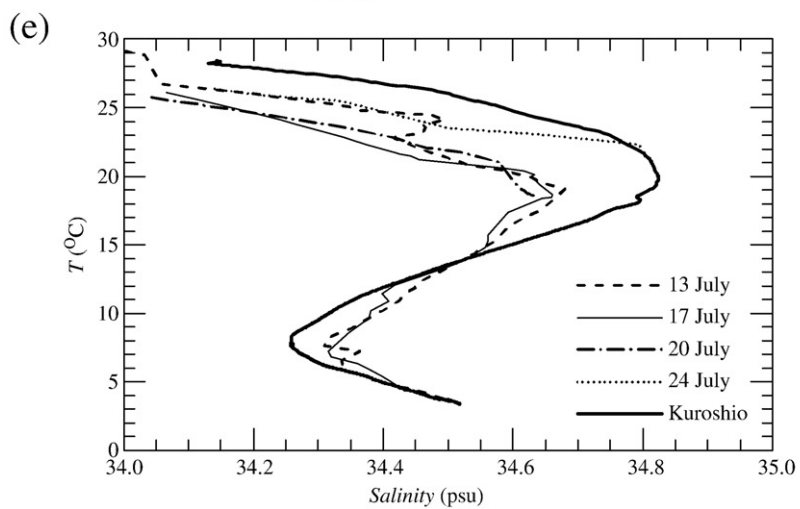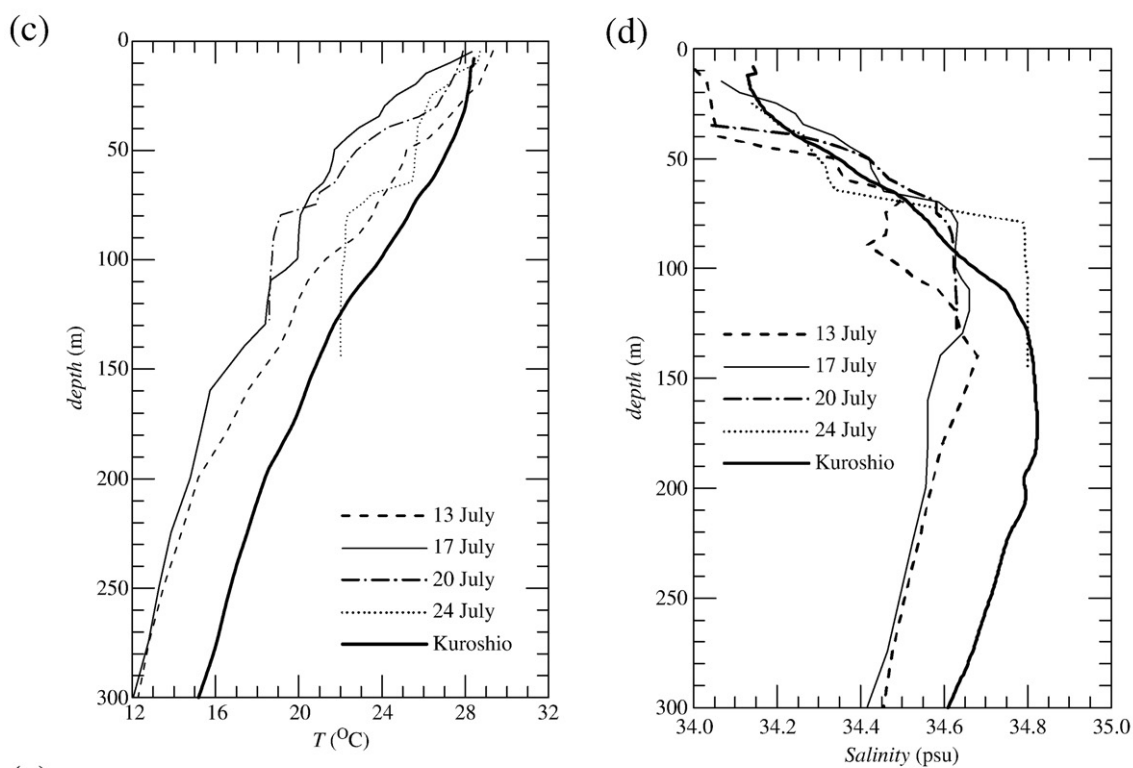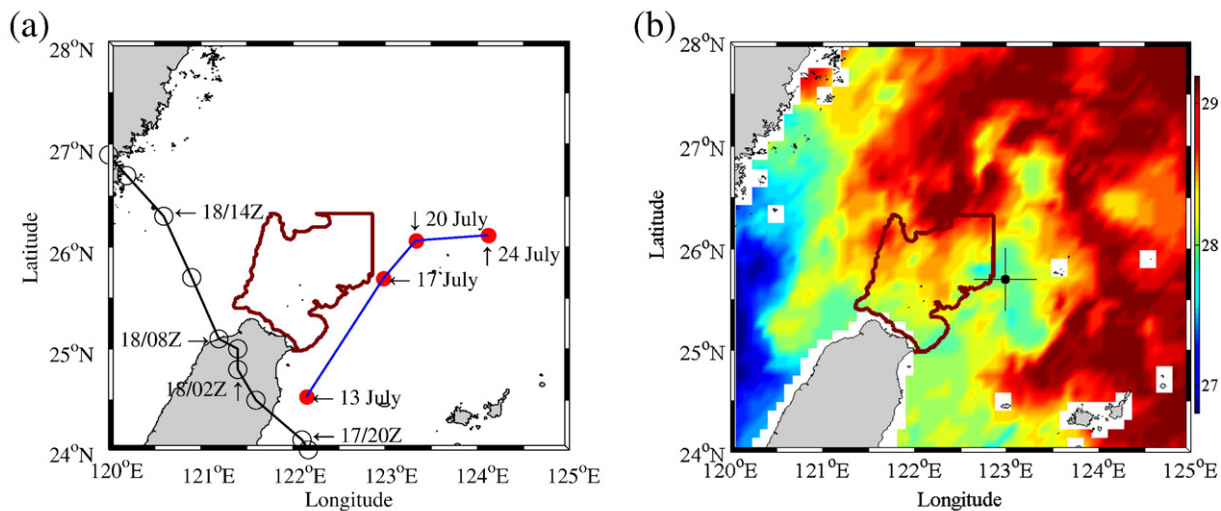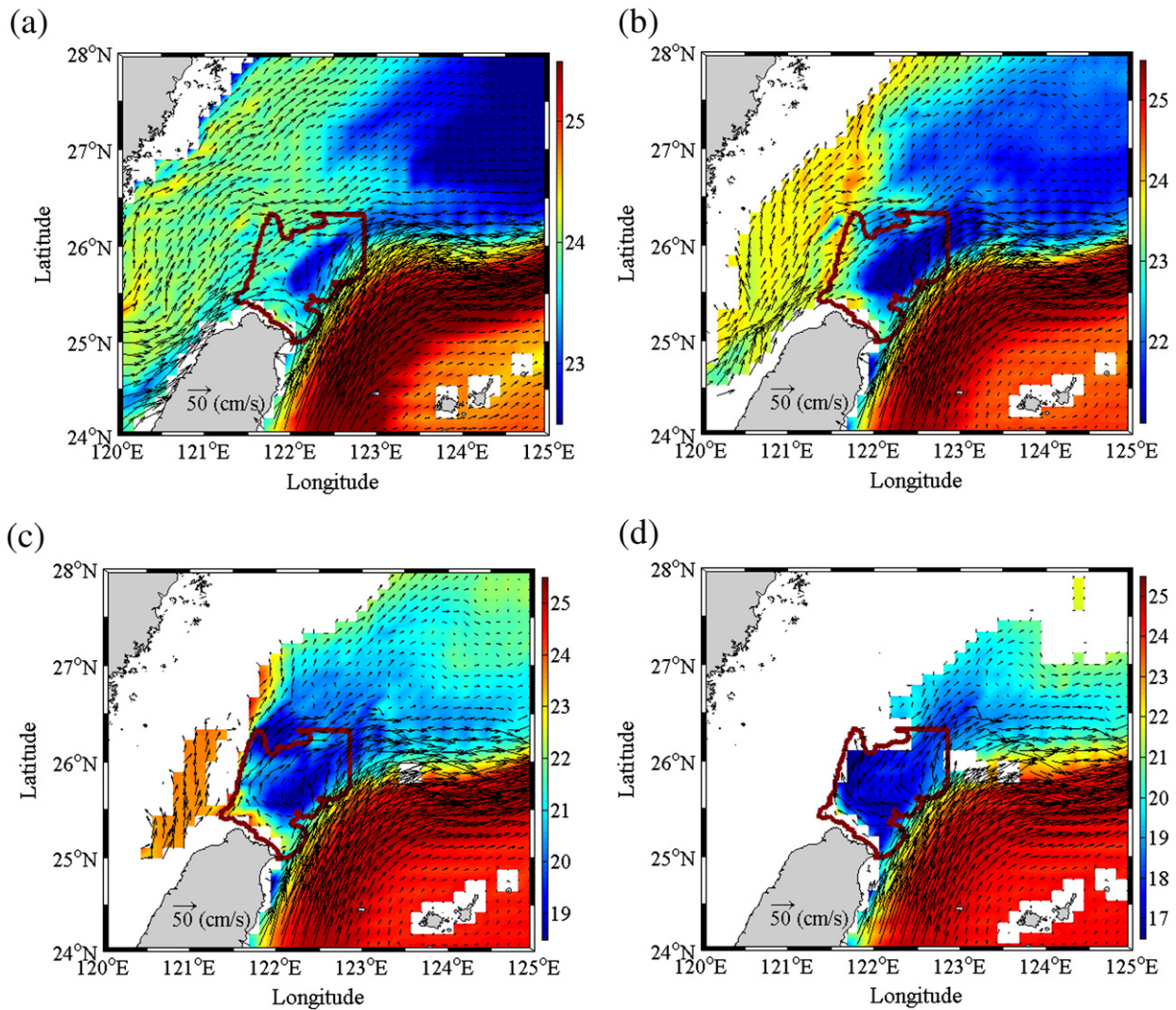
Fig. 7. Temperature distribution and horizontal velocities at (a) 6 m, (b) 54 m, (c) 75 m, and (d) 98 m deep, respectively averaged for Days 155–160, Year 37 of the model results.

4.1. A numerically reproduced cold-dome off northeast of Taiwan

Fig. 7 shows the temperature distribution and horizontal velocity fields at several depths (6 m, 54 m, 75 m, and 98 m) for a modeled cold-dome off northeastern Taiwan in summer, averaged over days 155–160 of Year 37. Note that the different color scales emphasize the temperature gradient at different depths. The cold-dome formed consistently in the model results, particularly in summer.

The modeled Kuroshio moved northward along the east side of Taiwan from 24°N, with the main axis located around 122.3°E (Fig. 7(a)). It turns abruptly eastward at around (25.5°N, 123°E), following the bathymetry contours, which are the continental shelf of the ECS. The warm and saline Kuroshio surface transport and the low salinity TSW converge at around (123°E, 26°N). In the south of the convergence zone, cold water exists displaying an evident cyclonic flow motion. This surface cyclonic circulation has been frequently reported in early field observations (Tang et al., 2000; Tang et al., 1999) and numerical modeling (Wu et al., 2008a).

The flow pattern at greater depth (for example, 54 m in Fig. 7(b)) is similar to the surface circulation. However, the cold-dome is more evident within the CDFR. The temperature increases monotonically

outward from the cold-dome center with the lowest temperature inside the CDFR. The cold water advects into the ECS at this depth, and in particular extends northeastward onto the shelf of the ECS.

At even greater depths, shown in Fig. 7(c) and (d), the extension of cold water and circulation suggests the typical topographical constraints of cold water within the CDFR. The large temperature gradient (about 2–3 °C) between the CDFR and ECS at these depths further indicates that the cold water is strongly constrained by the local topography off northeastern Taiwan and locked within the CDFR. The cold water inside the CDFR (about 18 °C and 16 °C at 75 and 98 m, respectively) also shows that the only water source that can be upwelled is the subsurface Kuroshio Water, KTW, because the other water sources (CW or KSW) contain no cold water that can be transported into this region.

4.2. Trajectories

We used the 3D Lagrangian trajectory diagnosis to investigate the routes of water masses around this region and their sources. The possible contributing water masses are KSW, KTW, Kuroshio Inter-mediate Water, ECS Water, CW, and TSW (Chen et al., 1995). The

Fig. 6. Argo data, WMOID 2900819, for (a) trajectory of the float within the study region; (b) MW and IR merged SST (the location of the Argo float on July 17, 2008 is marked as a circle). The subsurface temperature (c), salinity (d), and T–S profiles (e) are presented, in comparison with the hydrographic features of the Kuroshio main stream in summer. Typhoon Kalmaegi passed this region on July 17–18, 2008. The path of Typhoon Kalmaegi is also shown in (a).

hydrographic features of KSW, KTW, and TSW have already been discussed. The Kuroshio Intermediate Water is characterized by a salinity minimum while the ECS Water and CW are both depleted in nutrients. Three major water sources, KTW, KSW, and TSW, were further investigated in relation to the cold-dome (Chen et al., 1995). For simplicity, we released the tracers at the Kuroshio upstream on the zonal span along 24°N from 121.75°E to 122°E. The release depths were 6–60 m and 150–250 m, respectively. The former is used to trace the KSW and the latter the KTW. To analyze the source of the TSW, the tracers were released from the 24°N zonal section across the Taiwan Strait. These tracers were all released during Year 37 and were tracked until they flowed out of our area of interest or ran aground due to bathymetry.

The tracers released to track the KTW follow two major routes (Fig. 8(a)). One group flows onto the continental slope gradually, the other rapidly moves northeastward into the Okinawa Trough along the continental shelf. These trajectories also indicate that NMHC plays a key role in controlling the routes of KTW. They are all upwelled from a depth of 250 m (red color) to a depth of 100 m (light blue). This may result from collision with the zonally running shelf (Tang et al., 2000) and canyon effects (Allen and Durrieu de Madron, 2009). The majority of the KTW is effectively uplifted to 100 m and then trapped at around the same depth due to the circulation in the ECS. Note that only one third of the tracers (705 out of the 2080) are uplifted onto the continental shelf and reach a depth of 50 m. This indicates that only a third of water parcels here can be upwelled into the CDFR by Kuroshio flow advection.

The tracers released from the TSW (Fig. 8(b)) showed a wider span over the continental shelf and slope. Only a small part of the tracers drifted over the CDFR. Compared to the tracers released from KTW, only 13 trajectories out of a total of 1965 tracers released from TSW drifted over the CDFR and moved northward due to the cyclonic eddy off northeastern Taiwan. This indicates that the regional flow pattern off northeastern Taiwan may limit the intrusion of TSW. Furthermore, the vivid color change of the intruded tracers indicates that the TSW was mixed with the water mass in the CDFR at different depths and carried the exchanged hydrographic features into the ECS.

Finally, the tracers released from KSW (Fig. 8(c)) show two main trajectory groups. One follows the main Kuroshio and flows out of the area of interest into the Okinawa Trough. Some of these tracers may remain at around the same release depth and others may be transported to a deeper region (dark red) in the Okinawa Trough. The other group shows the intrusion of KSW, where the water parcels mostly remain in the surface region (blue color). Out of over 1770 trajectories, 144 are intruded into the ECS, mostly in winter.

5. Cold-dome formation mechanism

The ocean circulation generally follows the geostrophic balance with some adjustments. The regional circulation is heavily affected by boundary transport as well as the associated boundary mixing, geostrophic adjustment, and topographically controlled flow pattern. The surface cold water may come directly from the atmospheric heat flux, vertical upwelling, or horizontal advection. In the earlier sections, we addressed how the passage of typhoons is connected to the cold water in this area. However, the frequent occurrence of the cold-dome and its regional preference cannot result from the surface heat flux because the atmospheric influence is usually extensive. In this study, we mainly emphasize the fundamental formation mechanism in the ocean dynamics. Based on these guidelines, the cold-dome off northeastern Taiwan may be formed by the following possible mechanisms: (1) dynamic isotherm uplift due to the geostrophic balance near the western boundary (dynamic isotherm uplift hereafter) as shown in Fig. 9(a); (2) vertical mixing in the surface mixing layer; (3) Ekman upwelling as shown in Fig. 9(b) and
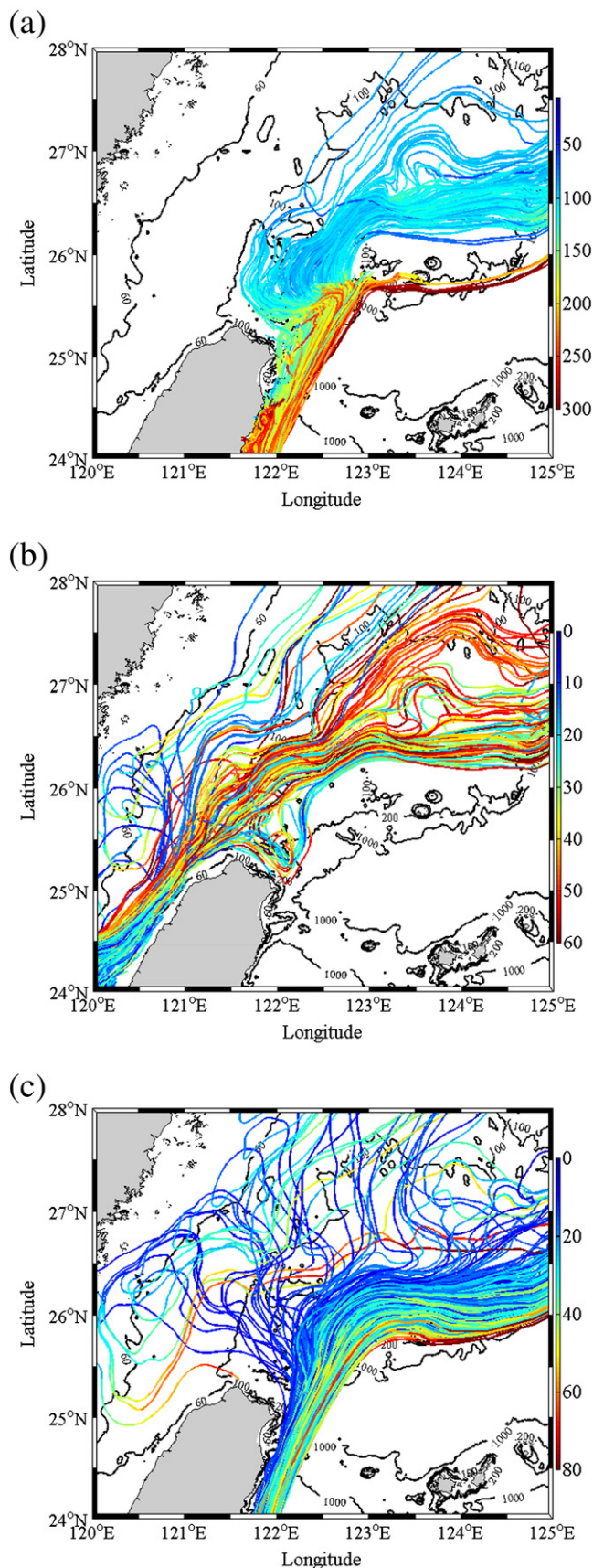

Fig. 8. Trajectories released from three water sources: (a) KTW, (b) TSW, and (c) KSW, respectively. The colors of tracers indicate the associated depths. The unit is the meter. Only one fourth of the valid trajectories are shown (see text for further details).
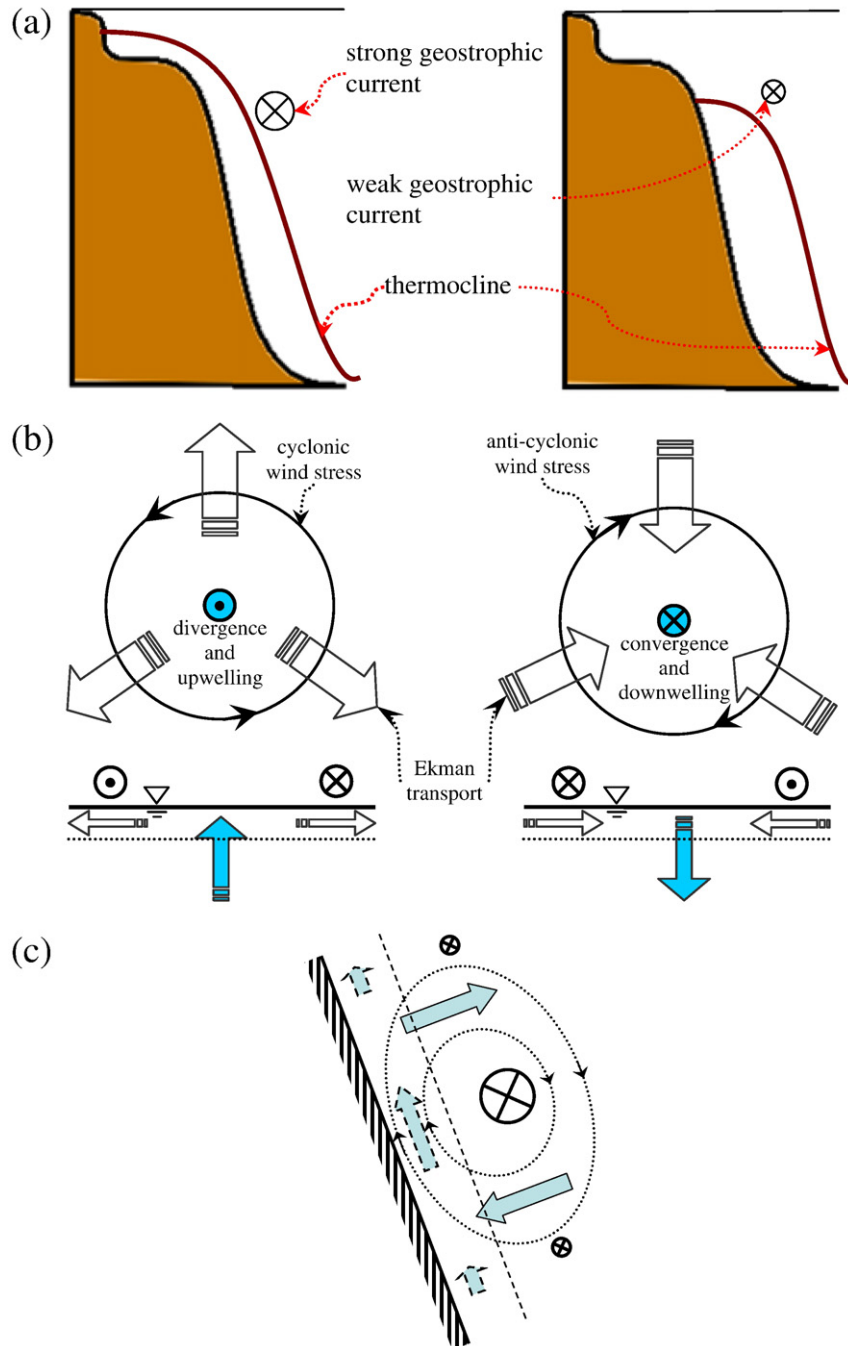
Fig. 9. Schematic of several dynamical mechanisms that may form the cold-dome: (a) geostrophic balance-induced isotherm uplift or so-called dynamic uplift; the left panel presents the higher uplift due to large the geostrophic current and the right panel the lower uplift due to the small geostrophic current; (b) surface Ekman transport of divergence (left) and convergence (right); and (c) boundary mixing due to Ekman boundary transport in the northern hemisphere. The circled cross and circled dot denote the direction of flow in and out the figure. The symbol size represents the current strength.

Ekman boundary mixing as shown in Fig. 9(c); and (4) topographically controlled upwelling. The dynamic uplift results from the geostrophic adjustment due to the balance of pressure gradient and the Coriolis force near the western boundary. Vertical mixing comes directly from ocean turbulence. The Ekman phenomena are due to the balance of the Coriolis force and boundary shear stress within the Ekman boundary layer, where the boundary thickness heavily depends on local eddy diffusivities. In this section, we analyze and evaluate these possible mechanisms in further detail.

Note that it is difficult to totally differentiate some contributions due to the multi-scale influences (in either space or time, from small to large) and their interactions. Nevertheless, they all result in a change in isothermal distribution. Therefore, we focus more on the distribution of isotherms rather than the upwelling velocities at specific locations.

5.1. Dynamic isotherm uplift

The most common oceanic uplift comes from the geostrophic balance along the western boundary, as shown in Fig. 9(a). This effect is called dynamic (isotherm) uplift (Tomczak, 2000), where the uplift height is based on the balance of pressure gradient as well as the Coriolis force and can be regarded as the linear dynamic of the western boundary currents. Therefore, the dynamic isotherm uplift

resulting from the geostrophic component of Kuroshio (geostrophic Kuroshio hereafter) in summer is expected to be larger than that in winter due to the variation in flow rate of Kuroshio and its seasonal axis migration (Tang et al., 1999, 2000).

Although the dynamic isotherm uplift suggests a change in the local isotherm, its influence cannot be determined exactly by theory. It may be further disturbed by surface non-geostrophic transport, topographically introduced current, and local energy transfer, either potential temperature or salinity. In this study, we traced the modeled 21 °C isotherm to investigate the influence of dynamic isotherm uplift. Fig. 10 shows the 21 °C isotherm depth with superimposed bathymetry. The entire water column warmer than 21 °C is not shaded. The greatest depth of the 21 °C isotherm in the region of interest is around 260 m, while the shallowest isotherm depth is around 40 m in CDFR.

A clear front closely follows the main Kuroshio axis (Fig. 10). This can be regarded as a reference of Kuroshio migration and is mainly due

to the dynamic isotherm uplift of geostrophic Kuroshio. As expected, Fig. 10(a) and (d) shows the onshore fronts when Kuroshio is moving shoreward, while Fig. 10(b) and (c) shows the offshore fronts when Kuroshio is moving seaward. The isotherm on the continental shelf resulted mainly from upwelling and will be discussed in Section 5.4.

To quantify the annual variation of dynamic isotherm uplift, we calculated the isotherm depth difference at two locations, (123.2°E, 24.2°N) and (121.9°E, 24.3°N), shown in Fig. 11 (dashed line), which were chosen to minimize the disturbance introduced by topographically induced flow and surface forcing. This isotherm uplift was compared with the Kuroshio transport (solid line) on PCM-1 and the surface pressure difference ΔP_{surf} (dashed line, 6 m depth in model results) shown in Fig. 11(b). The variation in ΔP_{surf} represents the geostrophic Kuroshio and agrees well (correlation of 0.86) with the Kuroshio flow rate except in winter (the northeast monsoon prevails and the associated surface geostrophic transport is strong). This
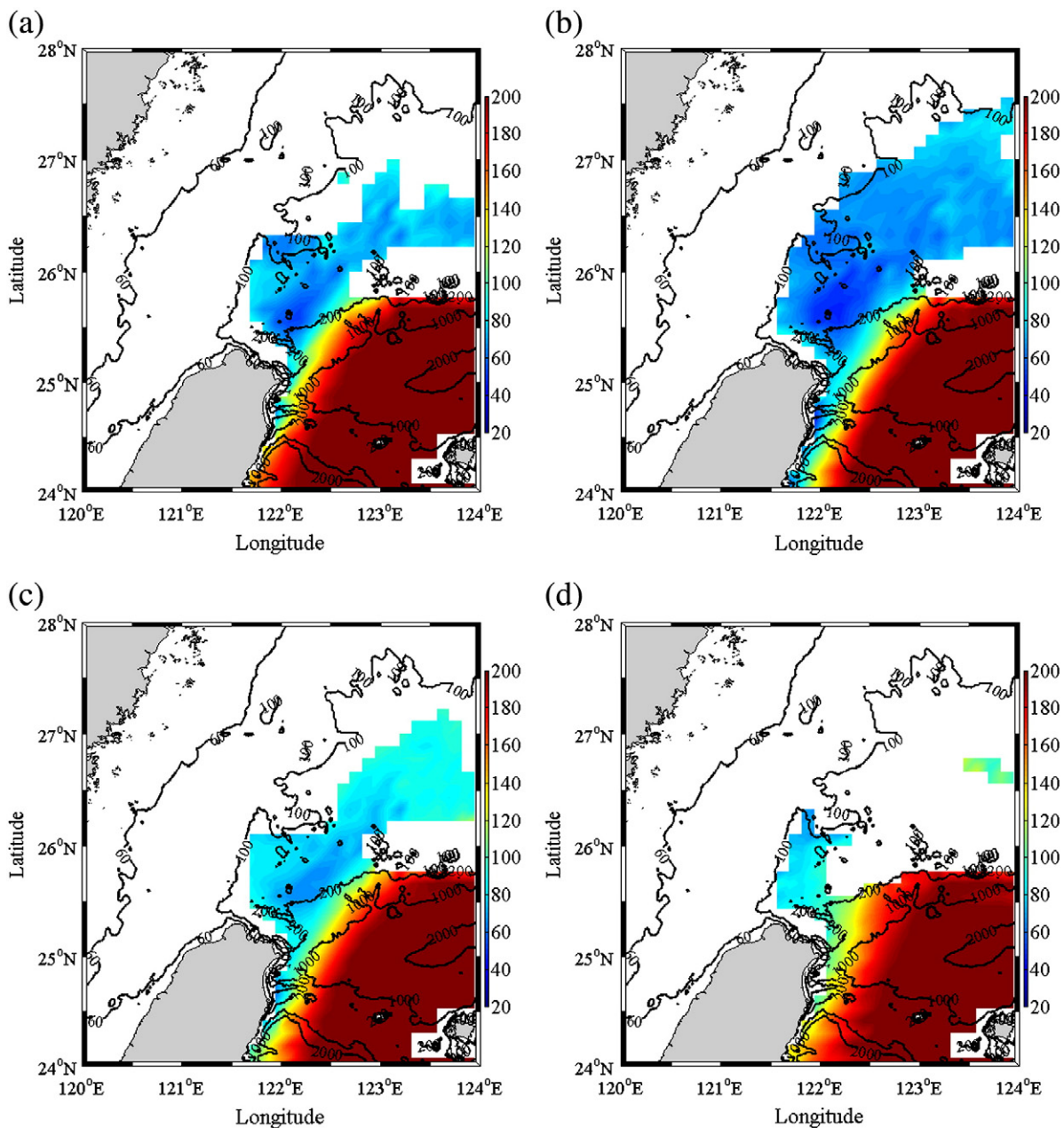

Fig. 10. The depths of the isotherm of 21 °C on: (a) Day 60, (b) Day 150, (c) Day 240, (d) Day 330, respectively. The whole water column warmer than 21 °C is not shaded. The unit is the meter.
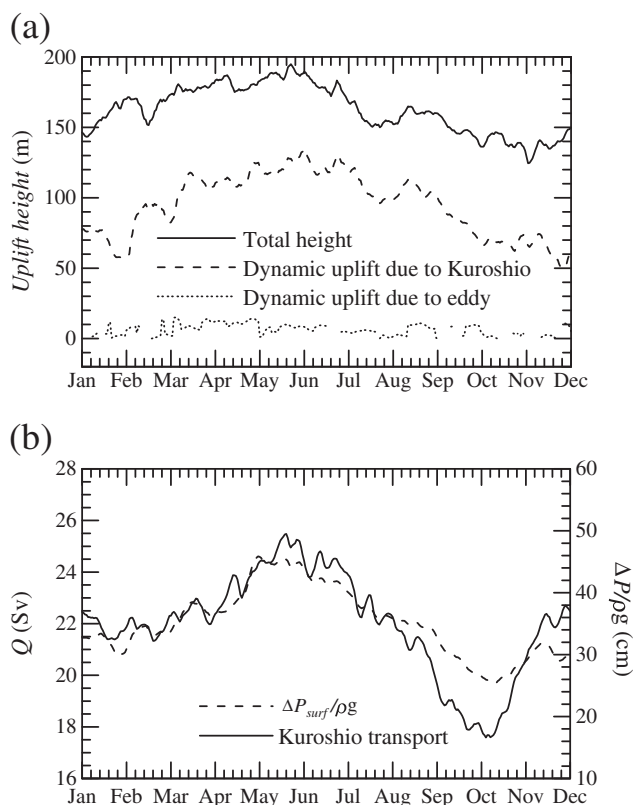
Fig. 11. (a) The total uplift height (solid line) and the dynamic uplift due to the Kuroshio (dashed line) and the cyclonic eddy (dotted line); (b) Kuroshio transport Q (dashed line) above the Ilan Ridge (PCM-1), and the surface pressure difference (6 m deep in the model results) of the two locations, (123.2°E, 24.2°N) and (121.9°E, 24.3°N).

difference causes a lower correlation of 0.56 between the Kuroshio transport and the isotherm uplift due to the indirect influence, whereas the correlation between ΔP_{surf} and the isotherm uplift is 0.88. Thus, this isotherm uplift is mainly introduced by the dynamic isotherm uplift due to the geostrophic balance of geostrophic Kuroshio along the western boundary.

Furthermore, the dynamic isotherm uplift indicates clear seasonal variation with a higher uplifted height in summer and a lower one in winter (the dashed line in Fig. 11(a)). Compared to the total uplift (solid line) in Fig. 11(a), which was determined by the difference between the maximum isotherm depth and the isotherm depth at (123.2°E, 24.2°N), we found that the seasonal pattern of the total isotherm uplift was supported by the dynamic isotherm uplift. Meanwhile, the dynamic isotherm uplift also dominates the annual variation in isotherm depth because the yearly averaged dynamic isotherm uplift is 92.8 m compared with the total yearly averaged uplift of 161.6 m (about 57.4% of the total isotherm uplift).

In addition to the dynamic isotherm uplift resulting from the geostrophic Kuroshio, the cyclonic eddy off northeastern Taiwan also suggests the other possible dynamic isotherm uplift (upwelling). This contribution can also be quantified numerically. Based on the geostrophic balance, the center of the cyclonic eddy has the local minimum in sea surface height (SSH), and its associated dynamic isotherm uplift (upwelling) can be defined as the difference between isotherms at the circulation center (SSH minimum) and in its surroundings (the dotted lines in Fig. 11). The dotted line indicates that the surface cyclonic eddy did not consistently exist, agreeing with field observations (Gong et al., 1992) and the model result of Wu et al. (2008a). Note that the dynamic isotherm uplift due to the cyclonic eddy can sometimes reach more than 15 m and has an annual mean of 5.3 m, contributing to 3.3% of the total isotherm uplift.

5.2. Vertical mixing of ocean surface boundary

Compared to advection, the mechanisms involved in the mixing layer are more complicated and difficult to quantify. Indeed, the contribution is also limited for the cold-dome formation. The Kuroshio dynamic isotherm uplift changes the thermocline along the continental break. The upwelling due to the cyclonic eddy can further uplift the isotherm depth on the continental slope, and the thermocline can tilt and form a dome shape as shown in Fig. 12(a). In the numerical simulation, the heat transfer due to vertical mixing can be quantified through the vertical turbulent eddy diffusivities (Fig. 12(b)). It is clear that the turbulent diffusion term, which decreases the surface temperature (Fig. 12(c)), also enhances the surface cold-dome formation resulting from strong vertical heat transfer.

5.3. Ekman upwelling and Ekman boundary mixing

The Ekman upwelling results from the boundary Ekman transport due to the balance between shear stress and the Coriolis force. The detailed horizontal and vertical formulae of Ekman transports used in this study are provided in the Appendix A. The climatological wind stress was applied to evaluate the wind-driven Ekman upwelling. Fig. 13 shows the Ekman transport at two locations, one within the cold-dome (121.1°E, 25.4°N) and the other near the edge of the Taiwan Strait (122.1°E, 25.5°N).

The wind-driven upwelling velocities inside the cold-dome and in the Taiwan Strait show similar variations except for a weak time lag, due to the migration of monsoon winds. The velocity magnitude agrees well with Chang et al. (2009), who suggest that wind-driven upwelling has an annual-averaged velocity of about −0.3 m/day (downwelling) with a variance of approximately 0.15 m/day. The Ekman transport causes convergence during the anti-cyclonic winter monsoon and causes divergence during the cyclonic summer monsoon (Fig. 9(b)). Our results are consistent with Chang et al. (2009) and indicate that the influence of Ekman upwelling is relatively small compared to the upwelling introduced by Kuroshio, and can be ignored.

In addition to the wind-stress, the stress due to the bottom boundary also suggests Ekman boundary transport near the bottom. Around MHC, a cyclonic circulation exists all year round, and therefore a current-driven Ekman transport was suggested for the topography near the bottom. However, based on the near bed current velocities and eddy diffusivities, the estimated magnitude in the model is only $O(10^{-5})$ m/day. Thus, current-driven Ekman pumping is insignificant.

Alongshore Ekman boundary transport is suggested by the balance of the alongshore velocity gradient of boundary current and the Coriolis force (Fig. 9(c)) (MacCready and Rhines, 1991, 1993; Romanou and Weatherly, 2001, 2004), which was reviewed (Garrett et al., 1993) and used to verify the upwelling of the East Australian Current (Roughan and Middleton, 2004). The boundary transport, either upwelling or downwelling, is counteracted by the buoyancy, resulting in Ekman boundary mixing and causing the redistribution of isopycnal (or isothermal) surfaces. Normally, the velocity gradient of near-shore Kuroshio suggests a strong Ekman boundary mixing to uplift isotherms. However, there is a counter-undercurrent along the continental break as the Kuroshio passes over the Ilan Ridge (in both summer and winter) (Tang et al., 2000). Thus, Ekman boundary mixing would suggest a slow downwelling velocity in the subsurface because the velocity gradient of the countercurrent is far smaller than that of Kuroshio. In such a case, Ekman boundary mixing can be ignored in the formation mechanism of the cold-dome.

5.4. Topographically controlled upwelling

Topographic upwelling is known to be an important mechanism in upwelling KTW to the continental shelf off northeastern Taiwan
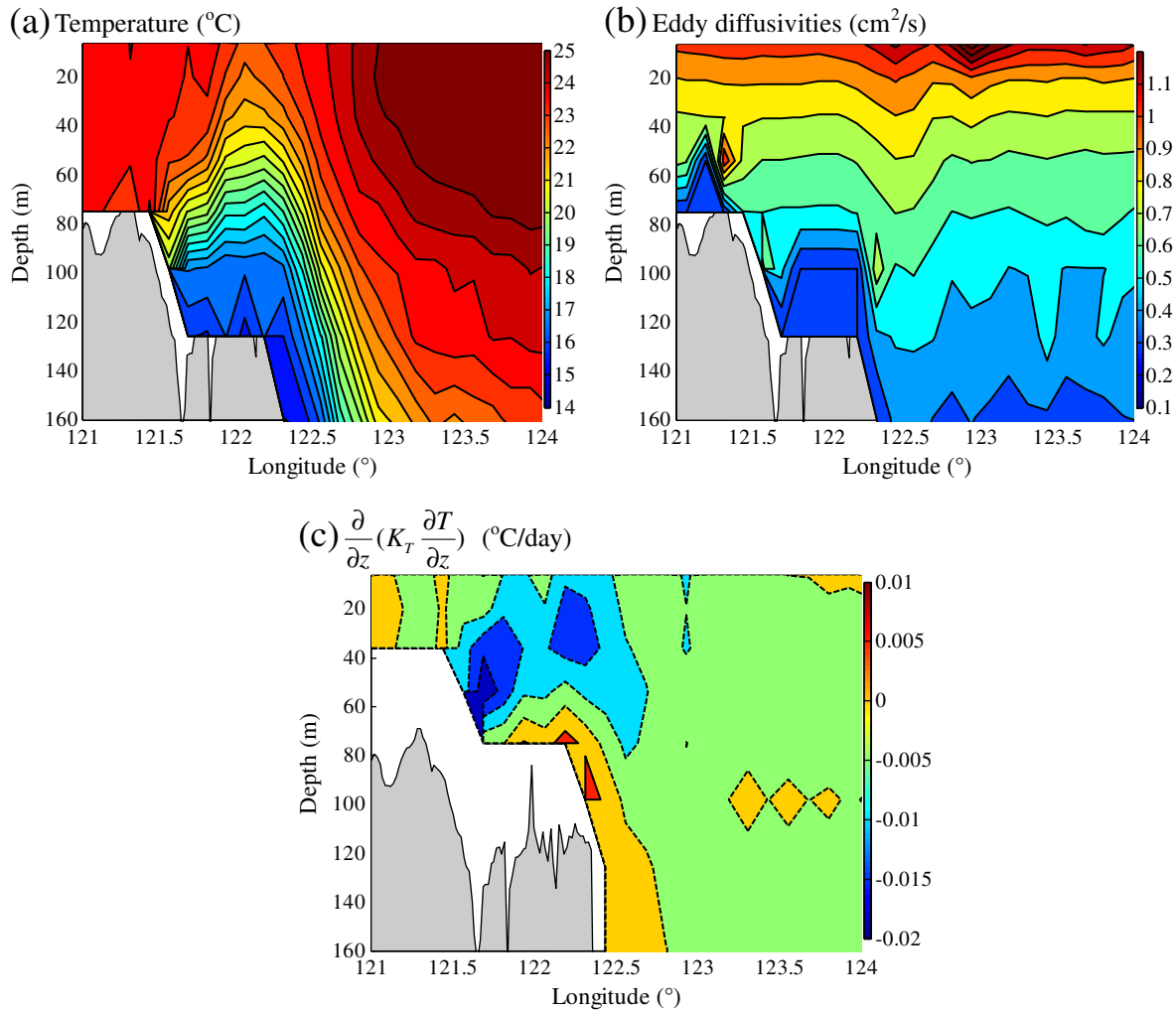
Fig. 12. Instantaneous zonal profiles of (a) temperature, (b) eddy diffusivities, and (c) the turbulent eddy diffusivity term in Eq. (4) at 25.6°N.

(Chang et al., 2009; Chern et al., 1990; Hu and Chang, 1992; Liu et al., 1992; Wong et al., 1991). Liu et al. (1992) employed a box model to analyze the downward flux of oxygen in the upwelling area and suggested that the upwelling velocity is approximately 5 m/day. While eliminating wind-driven Ekman pumping from the calculated vertical velocity in a specific region, Chang et al. (2009) suggested that the annually-averaged vertical velocity induced by Kuroshio is approximately 7.5 m/day. However, estimations based at a specific

location may be misleading because the contribution to upwelling is strongly affected by Kuroshio migration, Taiwan Strait outflow, and the shedding of the cyclonic eddy.

Another effective approach is to take into account the maximum uplift of the isothermal surface in the region of interest (solid line in Fig. 11). Note that the location of maximum uplift height may vary (Fig. 10) with the surrounding flow pattern and the associated upwelling mechanism. Apparently, the uplift difference between the maximum uplift height and the geostrophic contributed uplift results from several factors, including topographically induced upwelling, eddy-contributed dynamic isotherm uplift, vertical turbulent mixing, Ekman boundary transports, and others. Since the eddy-contributed dynamic isotherm uplift (upwelling) has an annual mean of 5.3 m and the Ekman boundary transport is insignificant in this area, the remaining isotherm uplift (changing the annual mean isotherm depth by up to 64 m) would mainly result from the topographically induced uplift, which dominates 39.6% of the total isotherm uplift.

The complicated bathymetry off northeastern Taiwan (Fig. 1(a)) not only suggests topographically induced upwelling, but also imposes the topographical constraints discussed in Section 4.1. Additional numerical experiments are performed to investigate the influence of bottom bathymetry. Fig. 14 compares the realistic bathymetry (RB) case with the other case, which removes or enhances the bathymetry of the annual-averaged results of Year 37.

The RB case in Fig. 14(a) shows a large cold-pool, centered at about 122.2°E, 25.7°N, off northeastern Taiwan. The cold water of the SB case
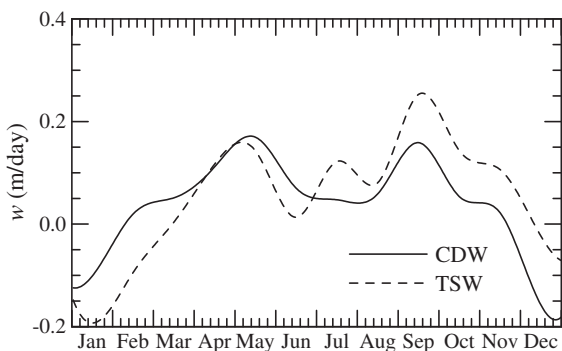

Fig. 13. The estimated vertical velocity generated from the wind-driven Ekman upwelling of the Taiwan Strait (dashed line) and of the cold-dome (solid line), in which the climatological wind stress and vertical eddy viscosity used in the model were applied. The velocities are calculated at 50 m deep by Eq. A3.
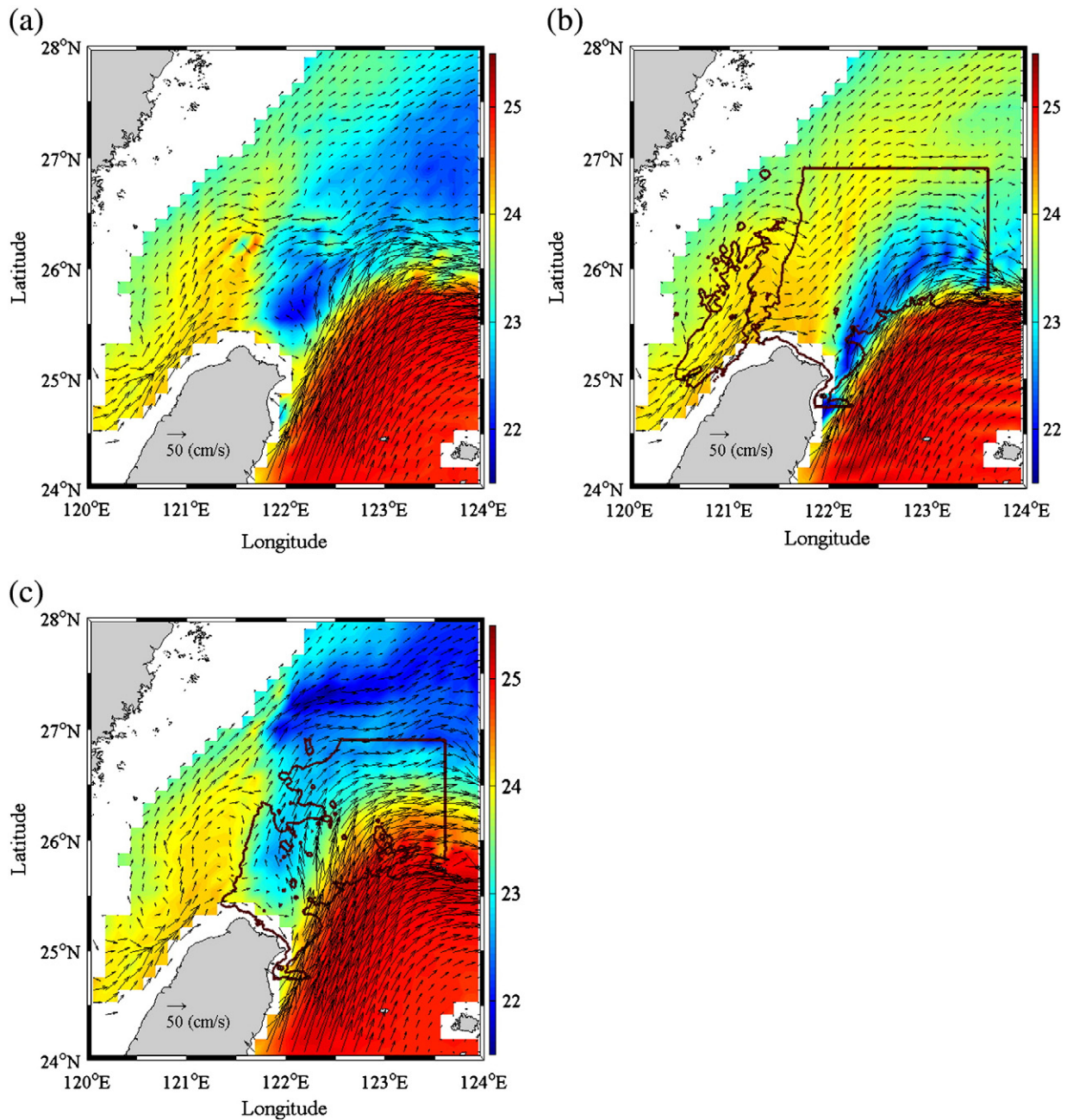
Fig. 14. Annual-averaged flow field and temperature distribution at 54 m using different topographies: (a) realistic bathymetry (RB); (b) shallow bathymetry (SB), in which the bathymetry is 80 m deep within the red encircled line; and (c) deep bathymetry (DB), in which the bathymetry is enhanced to 1.2 times the realistic bathymetry.

(Fig. 14(b)) is limited by the continental break and the flow exchange is reduced to the south of the ECS, and thus a larger amount of TSW flows northward, directly into the ECS. This confirms the island constraint of Taiwan on the resulting circulation pattern in the ECS (Pedlosky et al., 1997; Yang, 2007) and suppresses the appearance of the cyclonic eddy off northeastern Taiwan. In comparison, the cold water in the DB case (Fig. 12(c)) expands more into the ECS. This results in less cold water being constrained off northeastern Taiwan, and most of the cold water is then convected northward. The DB case also supports the enhancement of cold water through the dynamic isotherm uplift due to the geostrophic Kuroshio. Thus, the bathymetry off northeastern Taiwan not only contributes heavily to topographically induced upwelling but also constrains the cold water in CDFR, and therefore enriches the surrounding fishing ground.

6. Conclusions

The spatial and temporal SST anomaly suggested that the surface cold-dome was observed more frequently in summer, and included some cold water residual due to typhoon events. According to the observed SST fronts, we observed that seasonal and interannual variations exist in the filtered SST fields, indicating possible influences of the Kuroshio. A large salinity gradient at a depth of 60 m was found on December 12, 2008 on the edge of the NMHC, suggesting the fresh CW and saline KTW merged in the vicinity of northeastern Taiwan. Comparing with the averaged Kuroshio winter T–S profile, we observed that the near-shore thermocline can be uplifted about 85 m by the Kuroshio dynamic, and the saline KTW is upwelled along the canyons and is the source of the surface cold-dome.

Several possible formation mechanisms of the cold-dome off northeastern Taiwan were studied numerically using the DUPOM model. Based on the climatological forcing (without specific typhoons or cold fronts), the model results showed a clear cold-dome formation. By tracing the three major water masses (KSW, KTW, and TSW), we observed that the KTW has regularly upwelled onto the continental shelf along the canyons (including MHC and NMHC). Several well-known mechanisms were taken into account and analyzed through the change of isotherms. Three Ekman boundary effects, including wind-driven and current-driven Ekman transport and Ekman boundary mixing, were ruled out because the contribution was limited. We observe that the geostrophic Kuroshio can uplift the isotherm about 130 m from a depth of 250 m, forming a front that extends offshore from the east coast of Taiwan as shown in Fig. 10 and contributes significantly to the cold-dome formation and its seasonal occurrence (57.4% of the total isotherm uplift). The secondary contribution to the cold-dome formation is suggested to come from the topographically controlled upwelling (39.6% of the total isotherm uplift). The dynamic of a cyclonic eddy can also uplift the annual mean thermocline by 5.3 m and contributes only 3.3% of the total isotherm uplift. The turbulent mixing seems to play a minor role in the CDFR.

Acknowledgements

Appendix A

The surface Ekman phenomenon has been well-documented as the balance of wind stress and Coriolis force, and is theoretically dominated by the wind stress curl. For a known wind stress $\tau_o = (\tau^x, \tau^y)$, it has been shown that the horizontal velocities due to the Ekman phenomenon are as follows [Chang et al., 2009]

$$u_{wind}(\zeta) = \frac{e^\zeta}{\rho \sqrt{fA_v}} \left[\tau_o^x \sin\left(\zeta + \frac{\pi}{4}\right) + \tau_o^y \cos\left(\zeta - \frac{\pi}{4}\right) \right] \quad (A1)$$

$$v_{wind}(\zeta) = \frac{e^\zeta}{\rho \sqrt{fA_v}} \left[-\tau_o^x \cos\left(\zeta + \frac{\pi}{4}\right) + \tau_o^y \sin\left(\zeta - \frac{\pi}{4}\right) \right] \quad (A2)$$

where $\zeta = z/\delta_E$, in which $\delta_E = \sqrt{2A_v/f}$ is the thickness of the Ekman layer. Using the mass conservation, we can derive the Ekman upwelling velocity as below:

$$w_{wind}(\zeta) = \frac{1}{\rho f} \left[-(\nabla_h \cdot \tau_o) e^\zeta \sin(\zeta) + (\nabla_h \times \tau_o)\left(1 - e^\zeta \cos(\zeta)\right) \right] \quad (A3)$$

Since the wind stress, eddy viscosity, and temperature are known variables in our model, the wind-driven upwelling, w_{wind}, can be calculated.

References

Allen, S.E., Durrieu de Madron, X., 2009. A review of the role of submarine canyons in deep-ocean exchange with the shelf. Ocean Sci. Discuss. 6 (2), 1369–1406. doi:10.5194/osd-6-1369-2009.

Chang, Y.L., Wu, C.-R., Oey, L.Y., 2009. Bimodal behavior of the seasonal upwelling off the northeastern coast of Taiwan. J. Geophys. Res. 114 (C03027), 13. doi:10.1029/2008jc005131.

Chang, Y.-L., Oey, L.Y., Wu, C.-R., Lu, H.-F., 2010. Why are there upwellings on the northern shelf of Taiwan under northeasterly winds? J. Phys. Oceanogr. 40 (6), 1405–1417. doi:10.1175/2010JPO4348.1.

Chen, C.-T.A., 1996. The Kuroshio intermediate water is the major source of nutrients on the East China Sea continental shelf. Oceanolog. Acta 19 (5), 523–527.

Chen, C.-T.A., 2003. Rare northward flow in the Taiwan Strait in winter: a note. Cont. Shelf Res. 23 (3–4), 387–391.

Chen, C.-T.A., 2005. Tracing tropical and intermediate waters from the South China Sea to the Okinawa Trough and beyond. J. Geophys. Res. 110 (C5), C05012.

Chen, C.-T.A., 2008. Distributions of nutrients in the East China Sea and the South China Sea connection. J. Oceanogr. 64 (5), 737–751.

Chen, C.-T.A., 2009. Chemical and physical fronts in the Bohai, Yellow and East China seas. J. Mar. Syst. 78 (3), 394–410.

Chen, C.-T.A., Huang, M.-H., 1996. A mid-depth front separating the South China Sea water and the Philippine Sea water. J. Oceanogr. 52 (1), 17–25.

Chen, C.-T.A., Sheu, D.D., 2006. Does the Taiwan Warm Current originate in the Taiwan Strait in wintertime? J. Geophys. Res. 111 (C4), C04005.

Chen, C.-T.A., Ruo, R., Paid, S.-C., Liu, C.-T., Wong, G.T.F., 1995. Exchange of water masses between the East China Sea and the Kuroshio off northeastern Taiwan. Cont. Shelf Res. 15 (1), 19–39. doi:10.1016/0278-4343(93)E0001-O.

Chen, C.-T.A., Liu, C.-T., Chuang, W.-S., Yang, Y.-J., Shiah, F.-K., Tang, T.-Y., Chung, S.-W., 2003. Enhanced buoyancy and hence upwelling of subsurface Kuroshio waters after a typhoon in the southern East China Sea. J. Mar. Syst. 42 (1–2), 65–79. doi:10.1016/S0924-7963(03)00065-4.

Cheng, Y.-H., Ho, C.-R., Zheng, Z.-W., Lee, Y.-H., Kuo, N.-J., 2009. An algorithm for cold patch detection in the Sea off northeast Taiwan using multi-sensor data. Sensors 9 (7), 5521–5533. doi:10.3390/s90705521.

Chern, C.-S., Wang, J., Wang, D.-P., 1990. The exchange of Kuroshio and East China Sea shelf water. J. Geophys. Res. Oceans 95 (C9), 16017–16023.

Chuang, W.-S., Liang, W.-D., 1994. Seasonal variability of intrusion of the Kuroshio water across the continental shelf northeast of Taiwan. J. Oceanogr. 50 (5), 531–542. doi:10.1007/BF02235422.

Chuang, W.-S., Li, H.-W., Tang, T., Wu, C.-K., 1993. Observations of the countercurrent on the inshore side of the Kuroshio northeast of Taiwan. J. Oceanogr. 49 (5), 581–592. doi:10.1007/BF02237464.

Dietrich, D.E., Mehra, A., Haney, R.L., Bowman, M.J., Tseng, Y.-H., 2004. Dissipation effects in North Atlantic Ocean modeling. Geophys. Res. Lett. 31 (5), L05302. doi:10.1029/2003gl019015.

Dietrich, D.E., Tseng, Y.-H., Medina, R., Piacsek, S.A., Liste, M., Olabarrieta, M., Bowman, M.J., Mehra, A., 2008. Mediterranean Overflow Water (MOW) simulation using a coupled multiple-grid Mediterranean Sea/North Atlantic Ocean model. J. Geophys. Res. 113 (C7), C07027. doi:10.1029/2006jc003914.

Garrett, C., MacCready, P., Rhines, P., 1993. Boundary mixing and arrested Ekman layers: rotating stratified flow near a sloping boundary. Annu. Rev. Fluid Mech. 25 (1), 291–323. doi:10.1146/annurev.fl.25.010193.001451.

Gong, G.-C., Shyu, C.-Z., Shiu, W.-H., Liu, K.-K., 1992. Temperature fluctuation of the cold eddy off the northeast Taiwan: June–December. Acta Oceanogr. Taiwan. 28, 118–127.

Hellerman, S., Rosenstein, M., 1983. Normal monthly wind stress over the world ocean with error estimates. J. Phys. Oceanogr. 13 (7), 1093–1104.

Hsu, T.-Y., 2005. The temporal–spatial variation of bacterioplankton in the upwelling region, East China Sea. M.S. thesis, Institute of Oceanography, National Taiwan University, Taipei, Taiwan.

Hsueh, Y., 2000. The Kuroshio in the East China Sea. J. Mar. Syst. 24 (1–2), 131–139. doi:10.1016/S0924-7963(99)00083-4.

Hsueh, Y., Wang, J., Chern, C.-S., 1992. The intrusion of the Kuroshio across the continental shelf northeast of Taiwan. J. Geophys. Res. 97 (C9), 14323–14330. doi:10.1029/92jc01401.

Hsueh, Y., Chern, C.-S. and Wang, J., 1993. Blocking of the Kuroshio by the continental shelf northeast of Taiwan. J. Geophys. Res., 98(C7), 12351–12359, doi:10.1029/93jc01075.

Hu, J.-H., Chang, J.-L., 1992. The variability of hydrographic fields at Kuroshio's turning on northeast of Taiwan. Terr. Atmos. Ocean Sci. 3 (3), 277–292.

Isobe, A., 2008. Recent advances in ocean-circulation research on the Yellow Sea and East China Sea shelves. J. Oceanogr. 64 (4), 569–584. doi:10.1007/s10872-008-0048-7.

Isoguchi, O., Shimada, M., Sakaida, F., Kawamura, H., 2009. Investigation of Kuroshio-induced cold-core eddy trains in the lee of the Izu Islands using high-resolution satellite images and numerical simulations. Remote Sens. Environ. 113 (9), 1912–1925. doi:10.1016/j.rse.2009.04.017.

Jan, S., Tseng, Y.-H., Dietrich, D.E., 2010. Sources of water in the Taiwan Strait. J. Oceanogr. 66 (2), 211–221. doi:10.1007/s10872-010-0019-7.

Levitus, S., Boyer, T.P., 1994. Temperature. Vol. 4. World Ocean Atlas, 1994. NOAA Atlas NESDIS.

Lin, C.-Y., Shyu, C.-Z., Shih, W.-H., 1992. The Kuroshio fronts and cold eddies off northeastern Taiwan observed by NOAA-AVHRR imageries. Terr. Atmos. Ocean Sci. 3 (3), 225–242.

Liu, K.-K., Gong, G.-C., Lin, S., Yang, C.-Y., Wei, C.-L., Pai, S.-C., Wu, C.-K., 1992. The year-round upwelling at the shelf break near the northern tip of Taiwan as evidenced by chemical hydrography. Terr. Atmos. Ocean Sci. 3 (3), 243–275.

Liu, K.-K., Lai, Z.-L., Gong, G.-C., Shiah, F.-K., 1995. Distribution of particulate organic matter in the southern East China Sea: implications in production and transport. Terr. Atmos. Ocean Sci. 6 (1), 27–45.

Liu, C.-S., Liu, S.-Y., Lallemand, S.E., Lundberg, N., Reed, D.L., 1998. Digital elevation model offshore Taiwan and its tectonic implications. Terr. Atmos. Ocean Sci. 9 (4), 705–738.

MacCready, P., Rhines, P.B., 1991. Buoyant inhibition of Ekman transport on a slope and its effect on stratified spin-up. J. Fluid Mech. 223, 631–661. doi:10.1017/S0022112091001581.

MacCready, P., Rhines, P.B., 1993. Slippery bottom boundary layers on a slope. J. Phys. Oceanogr. 23 (1), 5–22.

Matsuno, T., Lee, J.S., Yanao, S., 2009. The Kuroshio exchange with the South and East China Seas. Ocean Sci. 5 (3), 303–312. doi:10.5194/os-5-303-2009.

Morimoto, A., Kojima, S., Jan, S., Takahashi, D., 2009. Movement of the Kuroshio axis to the northeast shelf of Taiwan during typhoon events. Estuar. Coast. Shelf Sci. 82 (3), 547–552. doi:10.1016/j.ecss.2009.02.022.

Naik, H., Chen, C.-T.A., 2008. Biogeochemical cycling in the Taiwan Strait. Estuar. Coast. Shelf Sci. 78 (4), 603–612.

Pacanowski, R.C., Philander, S.G.H., 1981. Parameterization of vertical mixing in numerical models of tropical oceans. J. Phys. Oceanogr. 11 (11), 1443–1451.

Pedlosky, J., Pratt, L., Spall, M., Helfrich, K., 1997. Circulation around islands and ridges. J. Mar. Res. 55, 1199–1251. doi:10.1357/0022240973224085.

Romanou, A., Weatherly, G.L., 2001. Numerical simulations of buoyant Ekman layers in the presence of variable stratification. Part I: Constant interior forcing. J. Phys. Oceanogr. 31 (10), 3096–3120.

Romanou, A., Weatherly, G.L., 2004. Numerical simulations of buoyant Ekman Layers. Part II: Rectification in zero-mean, time-dependent forcing, and feedback on the interior flow. J. Phys. Oceanogr. 34 (5), 1050–1066.

Roughan, M., Middleton, J.H., 2004. On the east Australian current: variability, encroachment, and upwelling. J. Geophys. Res. 109 (C7), C07003. doi:10.1029/2003jc001833.

Tang, T.-Y., Tang, W.-T., 1994. Current on the edge of the continental shelf northeast of Taiwan. Terr. Atmos. Ocean Sci. 5 (2), 335–348.

Tang, T.-Y., Hsueh, Y., Yang, Y.-J., Ma, J.-C., 1999. Continental slope flow northeast of Taiwan. J. Phys. Oceanogr. 29 (6), 1353–1362.

Tang, T.-Y., Tai, J.-H., Yang, Y.-J., 2000. The flow pattern north of Taiwan and the migration of the Kuroshio. Cont. Shelf Res. 20 (4–5), 349–371. doi:10.1016/S0278-4343(99)00076-X.

Tomczak, M., 2000. An Introduction to Physical Oceanographyonline source http://www.es.flinders.edu.au/~mattom/IntroOc/2000.

Tseng, Y.-H., Dietrich, D.E., Ferziger, J.H., 2005. Regional circulation of the Monterey Bay region: hydrostatic versus nonhydrostatic modeling. J. Geophys. Res. 110 (C9), C09015. doi:10.1029/2003jc002153.

Tseng, Y.-H., Jan, S., Dietrich, D.E., Lin, I.-I., Chang, Y.-T., Tang, T.-Y., 2010. Modeled oceanic response and sea surface cooling to Typhoon Kai-Tak. Terr. Atmos. Ocean Sci. 21 (1), 85–98. doi:10.3319/TAO.2009.06.08.02.

Tseng, Y.-H., Jan, S., Shen, M.-L., Dietrich, D.E. and Chiang, C.-P., 2011. Validation of the Kuroshio Current system in the dual-domain Pacific ocean model framework. Prog. Oceanogr. (accepted).

Udaya Bhaskar, T.V.S., Rahman, S.H., Pavan, I.D., Ravichandran, M., Nayak, S., 2009. Comparison of AMSR-E and TMI sea surface temperature with Argo near-surface temperature over the Indian Ocean. Int. J. Remote Sens. 30 (10), 2669–2684. doi:10.1080/01431160802555796.

Wong, G.T.F., Pai, S.-C., Liu, K.-K., Liu, C.-T., Chen, C.-T.A., 1991. Variability of the chemical hydrography at the frontal region between the East China Sea and the Kuroshio north–east of Taiwan. Estuar. Coast. Shelf Sci. 33 (2), 105–120. doi:10.1016/0272-7714(91)90001-R.

Wu, C.-R., Lu, H.-F., Chao, S.-Y., 2008a. A numerical study on the formation of upwelling off northeast Taiwan. J. Geophys. Res. 113 (C08025), 12. doi:10.1029/2007jc004697.

Wu, C.-R., Chang, Y.-L., Oey, L.-Y., Chang, C.W.J., Hsin, Y.-C., 2008b. Air–sea interaction between tropical cyclone Nari and Kuroshio. Geophys. Res. Lett. 35 (L12605), 7. doi:10.1029/2008gl033942.

Yang, J., 2007. An oceanic current against the wind: how does Taiwan island steer warm water into the East China Sea? J. Phys. Oceanogr. 37, 2563–2569. doi:10.1175/JPO3134.1.

Zheng, Z.-W., Ho, C.-R., Zheng, Q., Lo, Y.-T., Kuo, N.-J., Gopalakrishnan, G., 2010. Effects of preexisting cyclonic eddies on upper ocean responses to Category 5 typhoons in the western North Pacific. J. Geophys. Res. 115 (C9), C09013. doi:10.1029/2009jc005562.